Planetary and Space Science 127 (2016) 15–32

Contents lists available at ScienceDirect

Planetary and Space Science

journal homepage: www.elsevier.com/locate/pss

# Foreshock ions observed behind the Martian bow shock

R.A. Frahm [a,*], M. Yamauchi [b], J.D. Winningham [a], R. Lundin [b], J.R. Sharber [a], H. Nilsson [b], A.J. Coates [c]

[a] Southwest Research Institute, 6220 Culebra Road, San Antonio, TX 78228, USA
[b] Swedish Institute of Space Physics, Box 98128 Kiruna, Sweden
[c] Mullard Space Science Laboratory, University College London, Dorking, RH5 6NT, UK

ARTICLE INFO

*Article history:*
Received 1 February 2015
Received in revised form
9 November 2015
Accepted 20 December 2015
Available online 7 January 2016

*Keywords:*
Foreshock
Ions
Magnetosheath
Bow shock
Mars

ABSTRACT

The Mars Express Analyzer of Space Plasmas and Energetic Atoms experiment contains ion and electron instruments for conducting plasma measurements. On January 23, 2012, during in-bound travel of Mars Express in the southern hemisphere of Mars from its dawn side toward periapsis at dusk, the plasma instruments measured foreshock-like ion beams extending from outside the bow shock and into the magnetosphere, continuing to a distance of about a proton gyroradius from the bow shock. These ion beams were mostly protons, were observed to have energies greater than solar wind protons, and were not gyrating, in agreement with reflections of the solar wind proton beam. Furthermore, in the foreshock region the ion energy gradually decreased toward the magnetosheath, in agreement with an acceleration by outward-directed electric field in the bowshock. The observations also suggest that this electric field exists even inside the magnetosheath within the distance of a proton gyroradius from the bow shock.



## 1. Introduction

The solar wind forms a magnetospheric cavity around Mars. This magnetosphere results from an induced interaction of the solar wind with the upper atmosphere of Mars. The upper atmosphere of Mars ionizes and creates an ionosphere where currents flow to create the induced magnetic field. This causes the solar wind to be deflected around the planet. A shock is formed in front of the planet to deflect the solar wind around the planet. Between this bow shock and the ionosphere is a magnetosheath where the solar wind is diverted around the planet (Luhmann et al., 1995).

The solar wind fluctuates in velocity and density. Variations are observed over a wide range of time scales as the solar wind contains a variety of types of wave activity (Feynman, 1985). At Earth, factor of two pressure pulses of scale up to about 36,000 km wide have been observed in the solar wind which penetrate into the magnetosheath (Hietala et al., 2012). Inside the Earth's magnetosheath, plasmoids of higher momentum density than the surrounding plasma have been observed which can penetrate into the magnetoshere (Gunell et al., 2012). These observations coupled with the observations of waves in the magnetosheath of Mars (Espley et al., 2004, 2005; Winningham et al., 2006), all suggest a measure of similarity in the interactions of the solar wind with Earth and Mars.

Part of the solar wind interaction that creates the bow shock can create a foreshock region of reflected and accelerated electrons and ions. The foreshock is dependent on the interplanetary magnetic field (IMF) and its connection to the bow shock. When the angle between the IMF and bow shock normal is greater than 45°, the shock is quasi-perpendicular and the foreshock region is restricted to near the shock foot (Bale et al., 2005). For an angle less than 45°, the shock is termed quasi-parallel (Burgess et al., 2005) and the foreshock has a much larger domain. For quasi-parallel shocks, the electron foreshock is observed antisunward of the sunward-most IMF field line which connects to the bow shock (Eastwood et al., 2005; Yamauchi et al., 2011) with the ion foreshock more tailward than this location (see examples, Burgess, 1995, Figure 5B.1; Parks, 2004, Figure 10.11; Eastwood et al., 2005, Figures 2.1 and 2.3, Otto, 2006, Figure 6.9). Near the upstream boundary, separation between the electron and ion foreshock regions are related to the angle between the IMF and bow shock normal. It has been found at the Earth that this angle is less than 90° for electrons and less than 70° for ions, which is suggested by Burgess (1995) to be due to the acceleration mechanism for ions being less efficient than for electrons; however, the details may depend on the size and shape of the bow shock.

* Corresponding author. Tel.: +1 210 522 3855; fax: +1 210 522 4520.
*E-mail address:* rfrahm@swri.edu (R.A. Frahm).

http://dx.doi.org/10.1016/j.pss.2015.12.011

Foreshock ions are observed near the bow shock and can flow upstream of the planet in the solar wind; however, it is important to note that foreshock ions are observed in the foreshock region. The classifications of foreshock ions, which are both discrete and diffuse, are termed "reflected", "intermediate", and "diffuse" (Bale et al., 2005; Burgess et al., 2005; Pachmann et al., 1981). Foreshock ions have been explained by acceleration following reflections off the bow shock (Burgess and Schwartz, 1984; Oka et al., 2005; Yamauchi et al., 2015) and wave–particle interactions (Meziane et al., 2001; Mazelle et al., 2003). Reflection may take several forms including ion beams and ring distributions (Yamauchi et al., 2006, 2008, 2011, 2012) with energies several times the energy of the solar wind (Eastwood et al., 2005).

Eastwood et al. (2005) summarized observations of electron foreshock distributions as generated from electron beams or waves. Basically since the electron distribution is thermally dominated (as opposed to the kinetic energy-dominated ion distribution), foreshock electrons appear as a high energy tail on the main solar wind electron distribution, with more energetic electrons observed near the tangent to the shock and less energetic electrons deeper in the electron foreshock. Waves are also observed in the electron foreshock region, shifting frequency deeper in the electron foreshock compared to the tangent point. Thus, distinguishing between the addition of an electron beam and wave–particle interactions to the solar wind electron distribution is difficult.

As a special feature of Martian bow shock, where the proton kinetic gyroradius (about 1000 km) and the existence of cold protons of exospheric origin can no longer be ignored, the reflected solar wind ions cause multiple foot structures at the bow shock (the shock foot is where the magnetic field gradually increases in front of the main shock). Sometimes it is difficult to distinguish the reflected solar wind ions from the exospheric origin pick-up ions which form a ring distribution (Yamauchi et al., 2011, 2012). The ring ion distribution, seen at comets and in planetary magnetospheres (e.g. Coates, 2012 and references therein) is a unique feature seen in the Martian foreshock and is a result of the curvature of the Mars bow shock compared to the local ion gyroradius. In Yamauchi et al. (2011, 2012), the reflected ions have nearly the same energy from the bow shock boundary to about one gyroradius into the solar wind, indicating that the reflection (acceleration) process takes place inside the bow shock, but the internal processes and location were not discussed. With Mars Express (MEx), it is actually possible to trace such acceleration process inward from the bow shock thanks to the large proton gyroradius at Mars and the slow traverse velocity of the spacecraft (due to the low gravity of Mars).

In this paper we present results from observations of foreshock-like ions which were detected both in the classical foreshock region and are continually observed as the spacecraft passes inside the bow shock at Mars to at least 800 km inside the magnetosheath. We begin by briefly discussing the instrumentation which made the observations and how this instrumentation is orientated with respect to the solar wind and Mars. This is necessary to understand the observations, which are presented next, followed by a discussion of the possible sources of the observed foreshock-like ions. Lastly, investigations for the future are discussed.

## 2. Instrumentation

Plasma is measured on the Mars Express (MEx) spacecraft (Chicarro et al., 2004) by the Analyzer of Space Plasmas and Energetic Atoms (ASPERA-3) experiment (Barabash et al., 2004, 2006). ASPERA-3 contains four instruments, one measuring ions, one measuring electrons, and two measuring neutral particles. The electron and neutral measurements are conducted on a scanner. This study focuses on the measurement of the ions and electrons in the foreshock, bow shock, and magnetosheath.

Ions are measured by ASPERA-3 using the Ion Mass Spectrometer (IMA). IMA has a top hat energy deflection system coupled with an elevation analyzer at the entrance and a magnetic momentum analyzer at the exit. During its operation, IMA has undergone several operational changes. For the ion data used in this study, ions between 50 eV and about 20 keV are measured logarithmically in 66 energy steps and linearly below 50 eV to −20 eV in 30 steps. Thus, there are a total of 96 energy steps in an energy sweep measuring the ion spectrum. IMA measures ions in 360° of azimuth with 16 angular sectors, each 22.5° wide. In elevation, IMA measures ions from −45° to +45° when energies are above 50 eV in 16 elevation sectors, each about 5.6° wide. Below 50 eV, elevation scanning is disabled and the ions are measured from the central plane at 0° elevation about 5.6° wide. The momentum analyzer accelerates the energy-angle analyzed ion beam, sending it through an orange-section style magnetic field where the ions are separated by momentum and are detected in a 32 mass channel array. Ions up to 40 amu are collected by IMA, simultaneously. The entire energy-angle-mass array is accumulated in 192 s. Each energy-azimuthal angle scan at a single elevation angle occurs in 12 s.

Electrons are measured by ASPERA-3 using the Electron Spectrometer (ELS). ELS is a spherical top hat analyzer which is mounted on a scanner. For these data, the scanner angle was fixed so that the ELS and IMA central plane are roughly perpendicular. The ELS measures in a central plane of 360° with 16 azimuth bins, each 22.5° wide. Perpendicular to the central plane of ELS, the angular width is ±2°. For these data, ELS operated in its survey mode, where a 127 energy step spectrum is measured from 0.5 eV to about 20 keV logarithmically in 4 s.

Both the ion and electron data presented here have the background estimated and removed. In both cases, background is estimated by accumulating signals above 10 keV for a time period which is 300 s for ELS and 192 s for IMA. These accumulated signals are assumed to represent background noise within the microchannel plate (MCP) sensors for each instrument. Accumulated signals are normalized to the instrument's accumulation period and then subtracted from each measurement before scientific units are calculated.

## 3. Orientation

The spacecraft entered the Mars system on the dawn side in the southern hemisphere and preceded to periapsis on the dusk side of Mars at about 2343 UT. Figure 1 aids in visualizing the MEx trajectory. Shown are views in the Mars Solar Orbital (MSO) coordinate system in the MSO $X$–$Y$ (a), $X$–$Z$ (b), and $Z$–$Y$ (c) planes as well as in cylinderical coordinates. MSO distances are given in km and relate to the cylindrical radius $\rho = \mathrm{sqrt}(Y^2+Z^2)/R_{\mathrm{Mars}}$, where $R_{\mathrm{Mars}} = 3397$ km and the $X$ distance in the cylindrical Fig. 1d is given in Mars radii. The average locations of the bow shock and the Magnetic Pileup Boundary (MPB) (Vignes et al., 2000) are indicated on Fig. 3d. The average position of the bow shock occurs at about 2222 UT and the average position of the MPB occurs at about 2307 UT. The MPB is defined using a magnetometer and since MEx contains no magnetic field experiment, MEx can only define the Induced Magnetospheric Boundary (IMB) (Lundin et al., 2004) from the particle signatures. However, the MPB and IMB are very nearly colocated.

Magnetic anomalies are most extreme in the southern hemisphere at a planetodetic longitude of 180°, and reach the magnetic

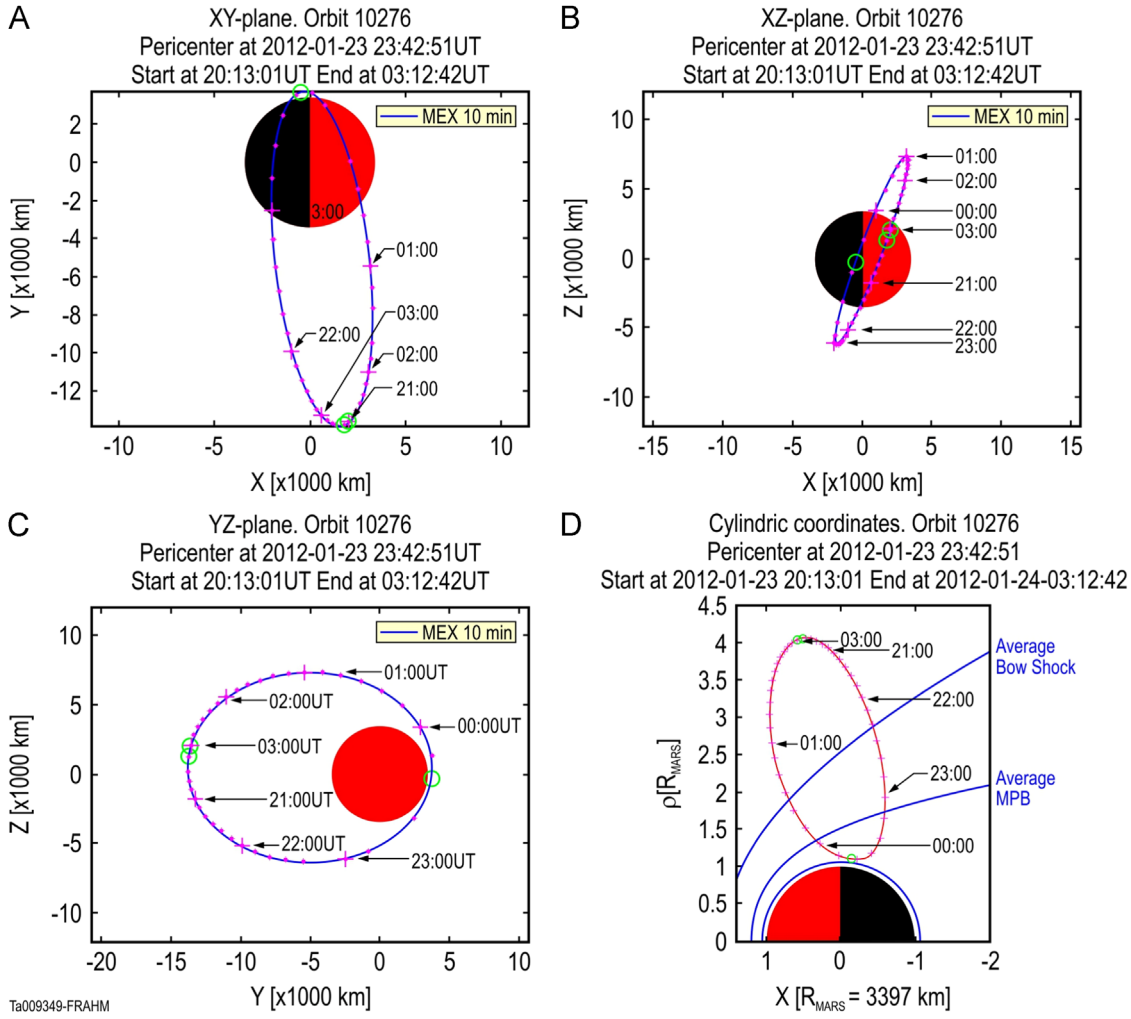


**Fig. 1.** Mars Express Trajectory on 23 January 2012. Shown are the trajectory of the Mars Express spacecraft in the *X*–*Y* (a), *X*–*Z* (b), and *Y*–*Z* (c) planes in km for the MSO coordinates for the pass of the spacecraft shown in Fig. 2. The Cartisian system is combined into a cylinderical representation and shown in terms of a Mars radii of 3397 km (d) with the central axis along the MSO *X* direction shown in the horizontal direction and the amplitude of the radial vector shown in the vertical direction. Two blue curves represent the average locations of the bow shock and Magnetospheric Pileip Boundary (MPB) (Vignes et al., 2000). In all panels, the location of the pericenter time is marked by a single green circle near the planet and the location of the apocenter time is marked with dual green circles indicating the beginning/ending definition of a MEx orbit.

equator in an arch fashion between 90° and 270° longitude (Connerney et al., 2001). The influence of the magnetic anomalies at bow shock distances affects the local standoff distance and the shape of the magnetic interaction (Frahm et al., 2008). Strong magnetic anomalies of the southern hemisphere can affect the bow shock location as the planet rotates, presenting different intensities and orientations of magnetic shielding to the solar wind. However, at the time of the MEx pass through the bow shock region, the magnetic distortion due to the configuration of magnetic anomalies was found to be a small contribution at bow shock distances. Since the average locations of the bow shock and MPB are similar to the measured locations of the bow shock and IMB, the solar wind dynamic pressure is probably similar to that determined as an average for Mars (Crider, et al., 2003), 0.75 nPa. As well, the Interplanetary Magnetic Field (IMF) intensity is probably about average as well (Brain et al., 2003), 2.75 nT. The contribution from magnetic anomalies is a fraction of 1 nT above the IMB, decreasing to less than a 10% effect at the bow shock. Thus, the influence of magnetic anomalies at the bow shock is treated as an insignificant and ignored. However, magnetic anomalies are significant at altitudes at and below the IMB, and cannot be ignored.

The solar wind ions are closely aligned with the Sun direction. For the time at which the data were taken between measurement of the solar wind at 2145 UT until measurement in the magnetosheath at 2240 UT, the Sun vector occurred at MEx between 78° and 84° in the spacecraft spherical polar angle, $\theta$. With the 22.5° azimuth sectors of IMA, the boundary between IMA azimuth sector 0 and sector 1 is at a spacecraft $\theta$ of 67.5°, so the solar wind ion beam should be strongest in IMA azimuth sector 0 with some smaller portion in IMA azimuth sector 1. In spacecraft azimuthal angle, $\varphi$, the Sun is located at 180° for the region of the bow shock. This translates to an IMA elevation angle of 0° (the central measurement plane), between elevation sectors 7 and 8.

During data collection from the region of the bow shock, the planet was located at a spacecraft polar angle between 0° and 0.1° with a spacecraft azimuth between 286° and 296°. Spacecraft mounting of IMA indicates that Mars is located in azimuth sector 11, very near its boundary with IMA azimuth sector 12, and near the central measurement plane at elevation sector 8, very close to the boundary with elevation sector 7.

Ions measured in azimuth sectors 0–1 and 14–15 are flowing in the solar wind direction ($-X_{MSO}$), 2–5 are flowing toward the planet ($+Z_{MSO}$, $+Y_{MSO}$), 6–9 are flowing toward the Sun ($+X_{MSO}$), and 10–13 are flowing away from the planet ($-Y_{MSO}$, $-Z_{MSO}$). The elevation orientation is more complicated due to the orientation of the spacecraft and the radial vector from the spacecraft to Mars. However in general, the gross orientation of elevation can be

taken as ions measured in elevation sector 8 and larger are flowing toward the MSO ecliptic plane while those elevations in sector 7 and smaller are flowing away from the MSO ecliptic plane because on the inbound portion of the orbit, MEx is in the MSO southern hemisphere.

## 4. Observations

As shown in Fig. 2, measurements begin in the solar wind at 2145 UT on January 23, 2012. Fig. 2 displays three panels. In the top panel, the background corrected electron spectra from sector 4 are shown in the energy (in eV) versus time (in UT) spectrogram format color coded in differential energy flux (in erg/(cm$^2$ s sr eV)). The center panel shows the ion spectrogram from sector 0 in energy (in eV) versus time (in UT) format color coded in differential energy flux (in erg/(cm$^2$ s sr eV)). In both cases, the color range is adjusted to highlight specific features within the spectrograms and the ranges of the color represent different values as noted on the color bars for each panel. The ion flux values less than 5.0e−7 ergs/(cm$^2$ s sr eV) have been removed to highlight the peak ion fluxes. The spacecraft planetodetic (Pd) altitude (Alt in km) and solar zenith angle (SZA in degree) is shown in the bottom panel and other orbital parameters are given in the labels at the bottom. These are the Cartesian *X*, *Y*, and *Z* position (in km) of the spacecraft in MSO coordinates, the planetodetic longitude (LON) and latitude (LAT) of the spacecraft (deg), and the solar time (SolTime in hr). MSO coordinates are defined at the center of Mars with the *X* axis pointing from Mars toward the Sun, the *Y* axis opposite the Mars orbital velocity vector, and the *Z* coordinate completing the right-hand orthogonal set. During this orbit, the MEx spacecraft was inbound from the solar wind in the southern hemisphere around dawn, reaching perigee on the dusk side of Mars near the equator in the northern hemisphere at about 350 km altitude

At the beginning of the pass, the ion spectral data suggested a steady solar wind at about 380 km/s. The red/yellow dots at about 750 eV (e.g. 2147:30 UT, 2150:45 UT, 2154 UT) are hydrogen ions and identified on the figure. The dot pattern occurs because the elevation analyzer measures ions as a function of time over a range of elevations and only encounters the solar wind proton beam at

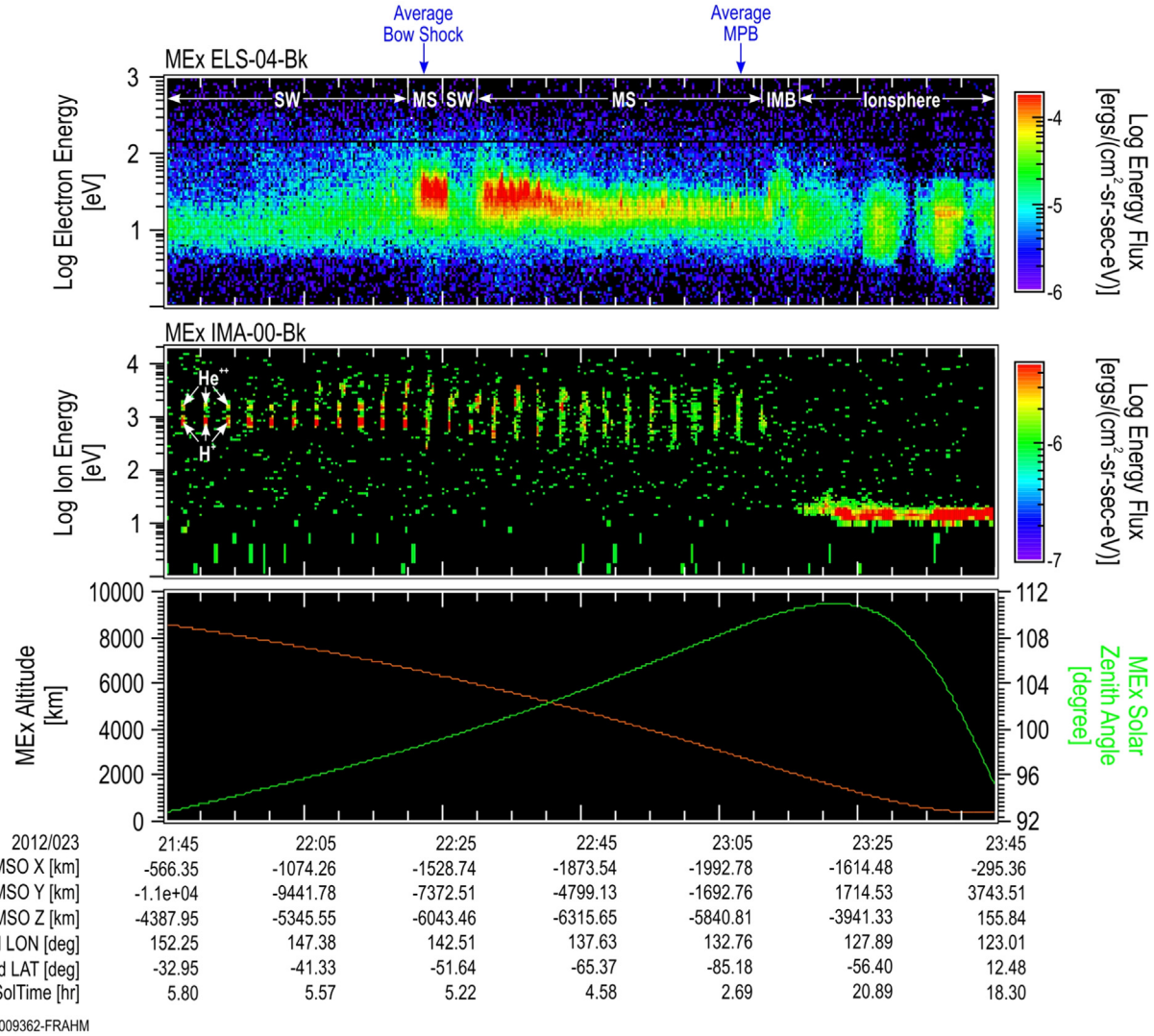


**Fig. 2.** Inbound charged particle measurements from the solar wind to periapsis. The top panel shows an energy-time spectrogram in differential energy flux of the ASPERA-3 electrons from ELS sector 04 with the plasma regions marked (SW = solar wind, MS = magnetosheath). The center panel shows an energy-time spectrogram in differential energy flux (DEF) of the ASPERA-3 ions from IMA sector 00 with the first three locations on solar wind ions noted. The bottom panel shows the spacecraft altitude and solar zenith angle with the position of the spacecraft in MSO *X*, *Y*, and *Z* (in km); Planetodetic longitude and latitude (deg); and solar time (h) given in the labels at the time markings listed. The average positions of the bow shock and MPS shown in Fig. 1d are indicated at the top. Both electron and ion spectra have background removed. Ion energy flux values below 5.0e−7 ergs/(cm$^2$ s sr eV) are excluded.

elevations near the central axis of the instrument. In this format, the helium ions in the solar wind shows as yellow/red peaks at the same elevations as the solar wind protons (the first three locations of the helium solar wind ions are shown on Fig. 2). Since the elevation scanning occurs above 50 eV and the solar wind ion beam is seen near the center of the elevation scan, low-energy ions in the solar wind should be observed below 50 eV during the elevation scan if the instrument threshold is exceeded. No low-energy ions are observed in the solar wind.

Background adjusted electron measurements indicate that the electron foreshock was detected beginning between 2157 UT to 2202 UT when the spacecraft was about 8000 km away from Mars. During this time, the solar wind electrons were observed to be stable and the core showed a slight increase in intensity from that in the solar wind; the halo/strahl electrons of the solar wind are observed to increase slightly. At about 2207 UT, foreshock-like ions were observed as a peak in the ion spectrum at higher energy than the solar wind $H^+$ and $He^{++}$, and at a different elevation angle with respect to the solar wind beam.

The average energy of the solar wind electron core was observed to increase in the foreshock. At about 2221 UT, a bow shock was encountered. The shocked solar wind core electrons were observed to increase in intensity by an order of magnitude over the solar wind flux and increase in average energy by about 20 eV. The shocked solar wind electrons were observed to decrease at about 2225:30 UT, where they returned to foreshock energy and intensity values. During this observation of shocked electron plasma, the ion measurements continue to show the solar wind ions, but also show ions at larger elevation angles which are separated from the solar wind ion population. These ions are flowing in the direction several degrees from the solar wind and possess a velocity component flowing away from the planet. In addition, the peak flux of the shocked electrons was observed to oscillate indicating the presence of wave activity.

Foreshock electrons again encountered a shock at about 2230 UT. Core electrons were shocked to the same flux values as observed previously with the same energy shift. Shocked ions were observed to disperse in angle around the central solar wind electron beam and the amount of dispersion increased as the spacecraft altitude decreased in the magnetosheath. As the magnetosheath was penetrated, the shocked electron core began to decrease in intensity after about 2239 UT. Throughout the magnetosheath, electron spectra indicated the presence of wave activity.

Between 2312 UT and 2316 UT, the IMB was encountered. This is marked by a transition between the shocked solar wind plasma and the planetary plasma (see example simulation of ion data

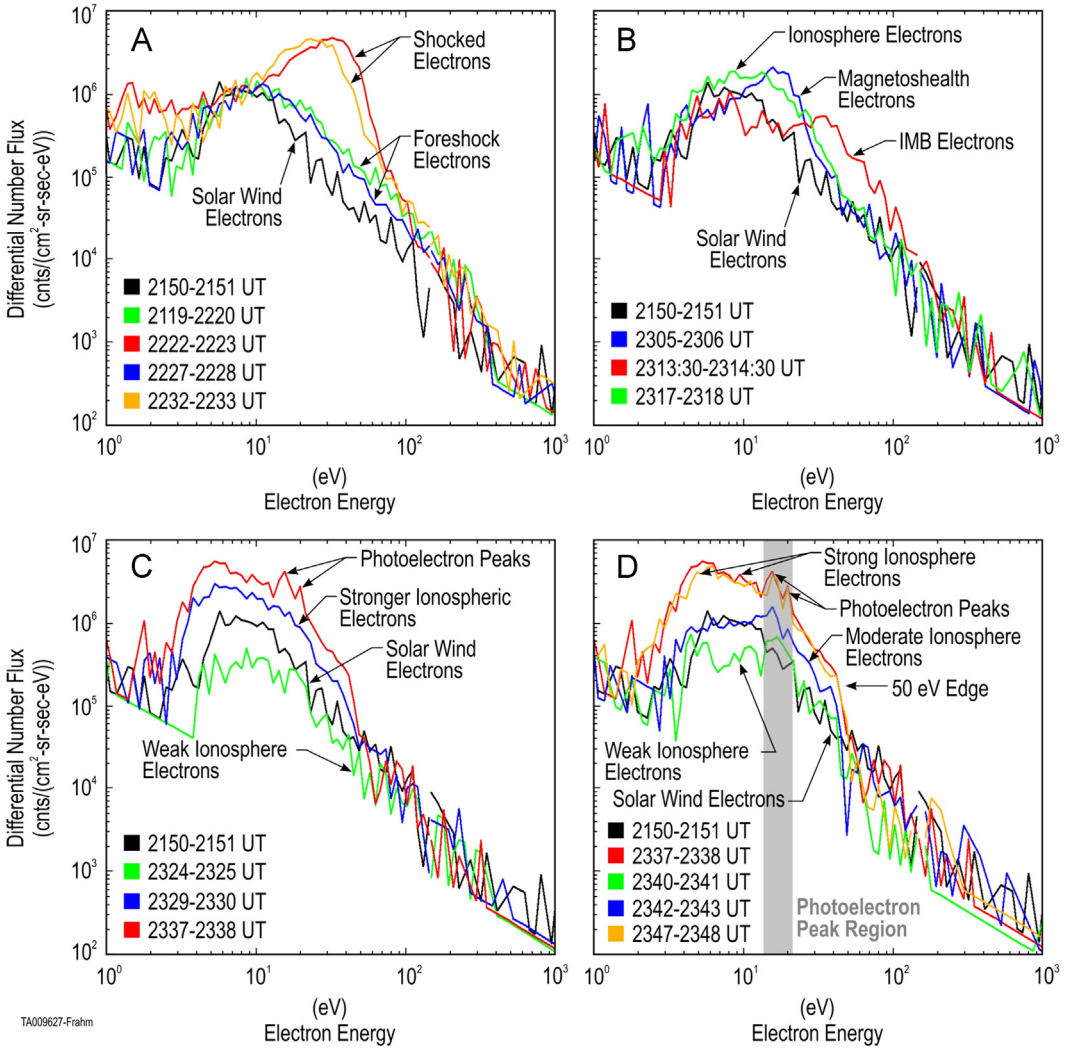


**Fig. 3.** Measured electron energy spectra at various locations from Fig. 2. The solar wind electron spectrum is shown on all panels as a reference. Panel A shows foreshock and shocked electron spectra from locations near the bow shock. Panel B shows electron spectrum from the IMB region. Panel C shows electron spectra from the topside ionosphere nearer to the IMB, whereas, Panel D shows electron spectra from lower altitudes in the ionosphere.

transition from ionosphere to magnetosheath in Kallio et al. (2008)). In this event, there was a distinct separation between the higher energy ion plasma above 50 eV (before 2312 UT) and the lower energy ion plasma below 50 eV (after 2316 UT). The ions before 2312 UT form the magnetosheath and were dominated by protons and helium. The ions after 2316 UT form the ionosphere and were dominated by heavy planetary ions. At the magnetosheath side of the IMB, as the altitude decreases, the electrons showed an increase in energy to nearly the same values as the heated core, but with flux values similar to those in the electron foreshock. These electrons form an inverted "V" shape with altitude/time. On the ionosphere side of the IMB, the electron temperature was similar to that in the solar wind above 50 eV; however, the plasma below 50 eV appeared to be similar to that in the ionosphere, exhibiting a broader differential number flux peak at lower energies. The electron flux decrease between 2324 UT and 2329 UT was due to a decrease in intensity as was the decrease between 2339 UT and 2342 UT, whereas, the electron flux decrease at 2330:30 UT resulted from a change in the spectrum, producing the signature of distinct dayside photoelectron peaks (Frahm et al., 2006a, 2006b, 2010) and the 50 eV ledge by 2332 UT resulting from ionization of the atmosphere.

Fig. 3 displays some electron spectra which have been averaged over 1 minute to improve statistics. Four regions are considered and all are drawn in differential number flux (electrons/(cm$^2$ s sr eV)) versus energy (eV). In all four panels, drawn in black, is the representative electron spectrum from the solar wind. It is useful to compare the solar wind spectrum to the electron spectrum from different plasma regions. The representative solar wind spectrum is taken as close to the apocenter as possible; however, this may still be in the electron foreshock region. Since MEx caries no magnetometer, the upstream solar region boundary cannot be determined.

Fig. 3a shows the electrons before the bow shock (green) and between magnetosheath plasma (blue). These spectra show a high energy tail consistent with the electron foreshock. Spectra from the magnetosheath region (orange and red) show an energized core population below 50 eV and the similar halo plasma above 50 eV to the foreshock electron population. Fig. 3b shows that magnetosheath plasma (blue) just before the IMB has a less intense core, but it still shows a similar shock feature and the similar halo compared to the solar wind spectrum. The electrons measured during passage through the IMB (red) show an accelerated spectrum higher in energy than the solar wind spectrum, between 20 and 100 eV in energy. The IMB electron spectrum shows that the halo population (greater than 50 eV) is not parallel to the solar wind halo population, indicating heating of halo electrons rather than just a change in density at the IMB. On the

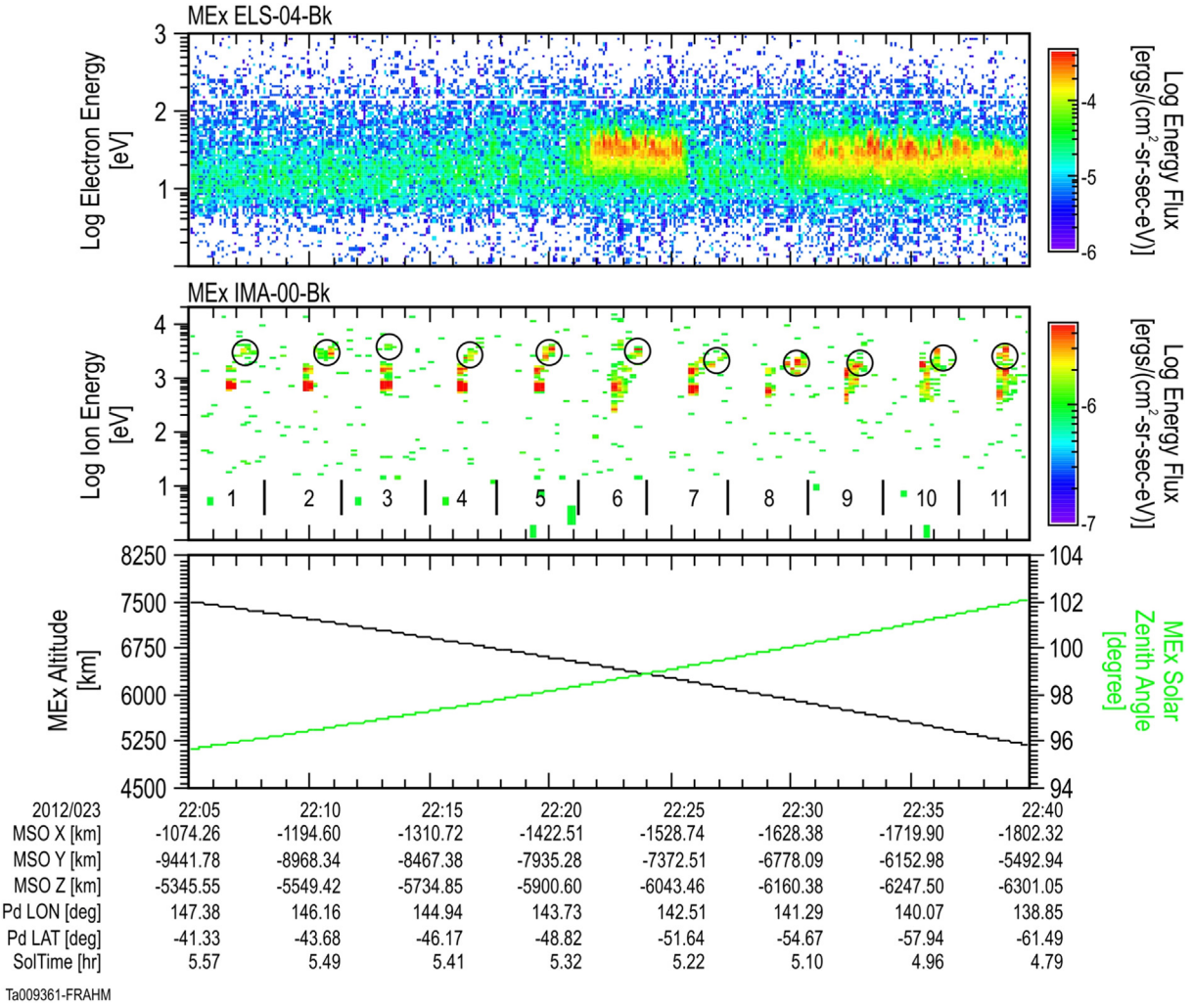


**Fig. 4.** Foreshock, Bow Shock, and the Outer Magnetosheath of Mars on 23 January 2012. The format is similar to Fig. 2, but the color range and time scale are adjusted to reveal more detail. The ion cycles of a complete energy-elevation scan are marked. The solar wind hydrogen is indicated as the red spot at the lowest energy for each measurement cycle. Foreshock-like ions are circled.

ionosphere side of the IMB (green), the spectrum has the intensity of the magnetosheath plasma, but includes a broader energy range than magnetosheath plasma and similar spectra in the halo region as the solar wind. Ionospheric spectra near the IMB can vary in intensity with some spectra greater (blue) and some less than (green) the solar wind spectra as indicated in Fig. 3c. As the spacecraft approaches the planet, peaks from the ionization of atomic oxygen and carbon dioxide appear in spectra (red). In the region around the pericenter (Fig. 3d), photoelectron peaks are commonly observed even though there can be over an order of magnitude difference in the peak intensity (blue=weak, green=moderate, red/orange=high flux intensity). The region in which photoelectron peaks are observed is indicated in Fig. 3d. In each case of electron spectra from the ionosphere in Fig. 3d, the aluminum edge in the electron spectrum at about 50 eV is observed.

## 5. Discussion

The region of interest is from the ion foreshock beginning at about 2205 UT and lasting until the ions penetrate the last bow shock at about 2240 UT. This region is highlighted in Fig. 4. The format of Fig. 4 is the same as in Fig. 2; however, the ion cycles are numbered in the ion spectrogram. Circles indicate observations of foreshock-like ions, i.e., ions with similar distribution and composition as discrete type foreshock ions observed with IMA in the Venus and Mars environments (Yamauchi et al., 2011, 2015). Foreshock ions are observed in the foreshock region. We use the term foreshock-like ions to indicate that ions are observed with similar properties to those in the foreshock region, but are observed beyond the foreshock region. Foreshock and foreshock-like ions are observed both flowing at an angle offset to that of the solar wind and at multiples of $H^+$ energies in the solar wind (these will be detailed later in Tables 1 and 2). Unfortunately since MEx carries no magnetometer, it cannot determine the deHauffman–Teller frame of the bow shock and estimate the shock normal direction. This pass shows no observed cyclic ions used to estimate the IMF direction and the deHauffman–Teller frame as in Yamauchi et al. (2006). Since the flow directions of these foreshock-like ions are narrowly distributed and relatively constant (Fig. 4), and since we know that the IMF is draped around the planet, so we estimate the IMF direction in the magnetosheath to be the direction of solar wind ion flow where we used the electron observations to determine the region of the magnetosheath. We

**Table 1**
Solar wind location within IMA. For each species and each instrument cycle, the largest solar wind differential number flux is highlighted in blue and the IMA azimuth-elevation pair is highlighted in yellow, indicating which IMA sector contains the major fraction of the solar wind.

| Instrument Cycle Number | Species | Energy (eV) | (Azimuth Sector, Elevation Sector) Pair | | | Number Flux at Peak ions/(cm$^2$ s sr eV) | | |
|---|---|---|---|---|---|---|---|---|
| 1 | H+ | 710 | (0, 7) | (1, 7) | | 1.53e4 | 7.42e3 | |
| | | | (0, 8) | (1, 8) | | 1.35e4 | 4.64e3 | |
| | He++ | 1440 | (0, 7) | (1, 7) | | 1.60e3 | 6.00e2 | |
| | | | (0, 8) | (1, 8) | | 8.25e2 | 4.64e2 | |
| 2 | H+ | 730 | (0, 7) | (1, 7) | | 1.29e4 | 5.74e3 | |
| | | 710 | (0, 8) | (1, 8) | | 1.38e4 | 5.87e3 | |
| | He++ | 1460 | (0, 7) | (1, 7) | | 2.35e3 | 3.75e2 | |
| | | 1410 | (0, 8) | (1, 8) | | 1.41e3 | 5.87e2 | |
| 3 | H+ | 750 | (0, 7) | (1, 7) | | 1.56e4 | 4.64e3 | |
| | | 760 | (0, 8) | (1, 8) | | 1.67e4 | 4.64e3 | |
| | He++ | 350-1590 | (0, 7) | (1, 7) | | 2.02e3 | 3.52e2 | |
| | | 1480 | (0, 8) | (1, 8) | | 1.70e3 | 5.16e2 | |
| 4 | H+ | 615-770 | (15, 7) | (0, 7) | (1, 7) | 2.56e3 | 1.60e4 | 4.95e3 |
| | | 700 | (0, 8) | (1, 8) | | 1.16e4 | 4.74e3 | |
| | He++ | 1200-1430 | (0, 7) | (1, 7) | | 2.72e3 | 3.23e2 | |
| | | 1450, 1310 | (0, 8) | (1, 8) | | 1.48e3 | 5.87e2 | |
| 5 | H+ | 700 | (15, 7) | (0, 7) | (1, 7) | 1.70e3 | 1.38e4 | 5.62e3 |
| | | 710 | (15, 8) | (0, 8) | (1, 8) | 3.10e3 | 1.74e4 | 9.45e3 |
| | He++ | 1400 | (0, 7) | (1, 7) | | 2.30e3 | 4.45e2 | |
| | | 1420 | (0, 8) | (1, 8) | | 1.60e3 | 5.87e2 | |
| 6 | H+ | 250 | (0, 7) | | | 1.00e4 | | |
| | | 350 | (0, 8) | | | 2.61e3 | | |
| | $He^{++}$ | 600-800, 780 | (0, 7) | (1, 7) | | 4.48e3 | 1.78e3 | |
| | | 520-900, 790 | (0. 8) | (1,8) | | 3.75e3 | 1.86e3 | |

**Table 1** (*continued*)

| Instrument Cycle Number | Species | Energy (eV) | (Azimuth Sector, Elevation Sector) Pair | | | Number Flux at Peak ions/(cm$^2$ s sr eV) | | |
|---|---|---|---|---|---|---|---|---|
| 7 | H+ | 625 | (15, 7) | (0, 7) | (1, 7) | 3.67e3 | 2.78e4 | 9.03e3 |
| | | 680 | (15, 8) | (0, 8) | (1, 8) | 1.29e3 | 5.74e3 | 1.98e3 |
| | He++ | 1350 | (0, 7) | | | 3.59e3 | | |
| | | 1410 | (0, 8) | | | 1.67e3 | | |
| 8 | H+ | 590 | (0, 7) | (1, 7) | | 7.58e3 | 8.80e3 | |
| | | 610 | (0, 8) | (1, 8) | | 2.84e3 | 1.67e3 | |
| | He++ | 1310 | (0, 7) | (1, 7) | | 1.19e3 | 1.70e3 | |
| | | 2000-1410 | (0, 8) | (1, 8) | | 7.91e2 | 1.26e3 | |
| 9 | H+ | 400-600 | (15, 7) | (0, 7) | (1, 7) | 1.70e3 | 7.9e3 | 2.4e3 |
| | | 700-800 | (15, 8) | (0, 8) | | 2.15e3 | 2.40e3 | |
| | He++ | 1100-4500 | (15,7) | (0, 7) | | 1.24e3 | 3.30e3 | |
| 10 | H+ | 600-750 | (15, 7) | (0, 7) | | 1.53e3 | 2.45e3 | |
| | | | (15, 8) | (0, 8) | | 2.25e3 | 3.03e3 | |
| | He++ | 1700, 1330 | (0, 8) | (1, 8) | | 5.05e3 | 1.11e3 | |
| | | 1100 | (14, 8) | (0, 8) | | 2.90e3 | 1.86e3 | |
| | | 1650 | (15, 8) | (0, 8) | | 2.30e3 | 1.24e3 | |
| 11 | H+ | 600, 550 | (15, 7) | (0, 7) | | 2.67e3 | 5.05e3 | |
| | | 450-500 | (15, 8) | (0, 8) | | 1.35e3 | 2.20e3 | |
| | He++ | 1100 | (0, 7) | | | 1.67e3 | | |
| | | 1400 | (0, 8) | | | 3.30e3 | | |

also know from Yamauchi et al. (2015) that the IMF is not very far away from the flow direction of foreshock-like ions; otherwise, depending on the angle to the solar wind, the flow direction of the foreshock ions should spread due to the gyromotion (Yamauchi et al., 2012). The exact mechanism for creating foreshock ions has not been identified; however, since the solar wind ions represent the only source of ions present, it is felt that foreshock ions are scattered solar wind ions, and thus, the flow direction differs from that of the solar wind. Multiples of solar wind energies are thought to be due to reflections of the solar wind in the deHaufmann–Teller frame, gaining a multiple of solar wind energy on each reflection.

Fig. 4 shows electron measurements that indicate three shock transitions at about 2221 UT, 2225:30 UT, and 2230 UT. Shocked plasma is observed in two segments and suggests that the spacecraft encountered conditions which caused an earlier bow shock at 2221 UT to be detected with penetration into the magnetosheath followed by a reverse shock (shocked plasma to unshocked plasma) at 2225:30 UT with solar wind plasma again observed. The bow shock transition observed at about 2330 UT indicates the spacecraft finally passing permanently into the magnetosheath. These transitions are also indicated by the ions as the solar wind $H^+$ indicates more heating at elevations around the solar wind $H^+$ beam when the solar wind penetrates into the magnetosheath (Lundin et al., 2006).

The angular deviation of ions are shown by examining three important energy ranges. These are 0.5–1 keV, 1–2 keV, and 2–5 keV, Fig. 5 indicates the instrument view of the ions in these three energy bands. In these angular presentations, along each vertical axis is shown the instrument azimuth rotated by 180° so that the solar wind appears in the center (0°–360°) and along each horizontal axis is shown the instrument elevation (−45° to +45°). Fig. 5 shows angular view spectrograms which correspond to the instrument cycles marked in Fig. 4. The approximate center time of the measurement cycle and the cycle number is indicated. The integral energy band 0.5–1 keV shows the angular location of the solar wind $H^+$ while the integral energy band 1–2 keV indicates mainly the solar wind $He^{++}$, but also shows some foreskock-like ions which are separated in angular space from the solar wind direction (indicated by arrows in Fig. 5). The 2–5 keV integral energy band shows foreshock and foreshock-like ions, separated from the solar wind both in energy and angle. Fig. 5 indicates that the foreshock-like ions appear closer to the solar wind direction and the solar wind $He^{++}$ energy the closer the spacecraft is to the planet. Angular differences between foreshock ions and the solar wind direction are on average 30°-40°. this means that the foreshock/foreshock-like ions are flowing toward the tail of Mars.

Conventional theory describing how foreshock ions are created is discussed in Yamauchi et al. (2015) and is illustrated in Fig. 6. Figure 6 represents a small portion of the bow shock where the solar wind ions (blue) are transmitted through and reflected off the bow shock, creating the fraction inside and flowing closer to the boundary to satisfy the shock jump conditions (Burgess, 1995; Parks, 2004) (blue). The fraction reflected becomes the foreshock population (purple). Parks (2004) and Yamauchi et al. (2006) describe how the electric field accelerates ions encountering the shock by a change in the cross product of the velocity of the particle and the magnetic field. The flow in the presence of the magnetic field generates an outward-

directed electric field in the bowshock. Creation of foreshock ions at multiples of the flow energy are generated in agreement with the observed foreshock ions Lastly, the approximate trajectory of the MEx spacecraft is nearly along the shock normal assuming average conditions as displayed in Fig. 1d, producing near normal measurements. It is not clear how foreshock-like ions are observed inside the magnetosheath without MEx observing a boundary causing reflection.

There are two possibilities for multiple observations of a boundary. The first is that the structure has a fixed physical shape which when projected along the spacecraft trajectory, the spacecraft passes in and out of the structure multiple times. The second is that the structure is temporal and the boundary passes across the spacecraft a multiple number of times. The MEx single spacecraft measurement means that spatial and temporal changes cannot be separated when measuring a single event. Moreover, structures repeated temporally may mask themselves as a fixed spatial structure under the right conditions. For a feature to be a permanent structure, multiple passes of the spacecraft through the same region will show a repeated pattern. No separate feature is observed on the outbound phase of this same orbit and the succeeding MEx passes through the Mars environment do not show this feature. In addition, there has not been a reported permanent structure in the bow shock region as shown in Fig. 4 suggesting the event is temporal rather than spatial. However, several cases of multiple bow shock crossings have been observed and are discussed under Section 6. So it is plausible that there exist multiple reflection surfaces closer to the planet than the outer most bow shock crossing. If the regions which show magnetosheath plasma farther from the planet than solar wind plasma as in 2225 UT to 2230 UT, there might be reflection off of the outer boundary where reflection of ions directs the foreshock component toward the planet as in Fig. 6. In this case, the spacecraft would block detection of these ions; and thus, in this case, MEx could not detect the reflected component.

The temporal–spatial structure in the bow shock/magnetopause region may also be a plasmoid or streamer which could be part of the bow shock structure (this includes a wavy bow shock) which is not a permanent feature. The bow shock boundary could surround magnetosheath plasma in the interior of the structure as it changes. Such a situation could be caused by a Kelvin–Helmholtz instability where there exists a flow velocity difference between plasma in the solar wind and magnetosheath, or a Raleigh–Taylor instability where the shocked plasma is compressed as it is diverted around the planet causing a density difference between

**Table 2**
Freshock ions. Excluding the solar wind for each instrument cycle, the most significant ion number flux peaks are examined and recorded. The peak energy as well as the energies at full-width-at-half-maximum (FWHM) are noted. The differential energy flux is estimated based on the center energy and differential number flux at the peak. The differential energy flux values are examined within an instrument cycle and the largest value is highlighted in blue. For selected instrument cycles, the second largest differential energy flux values are highlighted in yellow.

| Instrument Cycle Number | Species | Azimuth Sector | Elevation Sector | FWHM Low Energy (eV) | Energy at Peak (eV) | FWHM High Energy (eV) | Flux at Peak ions/(cm$^2$ s sr eV), ergs/(cm$^2$ s sr eV) |
|---|---|---|---|---|---|---|---|
| 1 | H+ | 15 | 10 | 2800 | 3400 | 3550 | 9.74e2, 5.31e-6 |
| | H+ | 0 | 10 | 2820 | 3100 | 3600 | 4.74e2, 2.36e-6 |
| 2 | H+ | 15 | 9 | 3060 | 3150 | 3730 | 5.62e2, 2.84e-6 |
| | H+ | 0 | 9 | 3000 | 3150 | 3830 | 3.75e2, 1.90e-6 |
| | H+ | 15 | 10 | 2500 | 2620 | 3300 | 4.84e2, 2.03e-6 |
| | H+ | 0 | 10 | 2320 | 2620 | 3420 | 3.52e2, 1.48e-6 |
| | H+ | 15 | 12 | 2620 | 3110 | 3500 | 1.78e3, 8.87e-6 |
| | H+ | 0 | 12 | 2590 | 2880 | 3450 | 1.00e3, 4.62e-6 |
| | H+ | 2 | 12 | 2600 | 2880 | 3450 | 4.64e2, 2.14e-6 |
| 3 | H+ | 15 | 8 | 3580 | 3720 | 4150 | 3.37e2, 2.01e-6 |
| | H+ | 0 | 8 | 3280 | 3720 | 4160 | 2.72e2, 1.62e-6 |
| | H+ | 15 | 9 | 3620 | 3700 | 3890 | 5.16e2, 3.06e-6 |
| | H+ | 0 | 9 | 3560 | 3700 | 3830 | 2.02e2, 1.20e-6 |
| 4 | H+ | 15 | 8 | 2360 | 2410 | 2390 | 2.11e3, 8.56e-6 |
| | H+ | 0 | 8 | 2270 | 2410 | 2530 | 1.04e3, 4.02e-6 |
| | H+ | 15 | 9 | 2200 | 2400 | 3450 | 7.42e2, 2.86e-6 |
| | H+ | 0 | 9 | 2250 | 2400 | 3170 | 6.67e2, 2.57e-6 |
| | H+ | 15 | 10 | 2890 | 2880 | 3100 | 1.04e3, 4.80e-6 |
| | H+ | 0 | 10 | 2720 | 2880 | 3150 | 5.50e2, 2.54e-6 |
| 5 | H+ | 15 | 9 | 2800 | 2620 | 3460 | 1.60e3, 6.72e-6 |
| | H+ | 0 | 9 | 2190 | 2620 | 3110 | 9.38e2, 3.94e-6 |
| | H+ | 2 | 9 | 2000 | 2620 | 3420 | 3.23e2, 1.36e-6 |
| | H+ | 0 | 10 | 3080 | 3900 | 3800 | 9.79e2, 6.12e-6 |

**Table 2** (*continued*)

| Instrument Cycle Number | Species | Azimuth Sector | Elevation Sector | FWHM Low Energy (eV) | Energy at Peak (eV) | FWHM High Energy (eV) | Flux at Peak ions/(cm$^2$ s sr eV), ergs/(cm$^2$ s sr eV) |
|---|---|---|---|---|---|---|---|
| 6 | H+ | 15 | 8 | 3600 | 3710 | 4100 | 1.82e2, 1.08e-6 |
| | H+ | 0 | 8 | 3500 | 3710 | 4850 | 4.45e2, 2.65e-6 |
| | H+ | 0 | 11 | 2240 | 2880 | 3020 | 5.05e2, 2.33e-6 |
| | H+ | 0 | 12 | 2600 | 2870 | 3030 | 6.53e2, 3.01e-6 |
| | H+ | 0 | 12 | 3300 | 3420 | 3530 | 9.18e2, 5.04e-6 |
| 7 | H+ | 15 | 8 | 1630 | 2020 | 2190 | 5.87e2, 1.90e-6 |
| | H+ | 0 | 8 | 1630 | 1720 | 2120 | 6.26e2, 1.73e-6 |
| | H+ | 14 | 9 | 1100 | 1210 | 1250 | 1.41e3, 2.74e-6 |
| | H+ | 15 | 9 | 2120 | 2210 | 2310 | 1.38e3, 4.89e-6 |
| | H+ | 15 | 9 | 4210 | 4910 | 5120 | 2.67e2, 2.10e-6 |
| | H+ | 0 | 9 | 2000 | 2210 | 2350 | 7.58e2, 2.69e-6 |
| | H+ | 15 | 10 | 1570 | 1690 | 1780 | 1.44e3, 3.90e-6 |
| | H+ | 0 | 10 | 1570 | 1690 | 1780 | 8.43e2, 2.29e-6 |
| | H+ | 2 | 10 | 1570 | 1690 | 1740 | 4.95e2, 1.34e-6 |
| | H+ | 15 | 11 | 1570 | 1700 | 1970 | 2.50e3, 6.82e-6 |
| | H+ | 0 | 11 | 1500 | 1880 | 1970 | 1.14e3, 3.44e-6 |
| | H+ | 2 | 11 | 1570 | 1700 | 1760 | 9.53e2, 2.60e-6 |
| | H+ | 15 | 12 | 1470 | 1550 | 1680 | 1.10e3, 2.74e-6 |
| | H+ | 0 | 13 | 2050 | 2400 | 2550 | 4.84e2, 1.86e-6 |
| | H+ | 0 | 14 | 2340 | 2620 | 2870 | 4.54e2, 1.91e-6 |
| 8 | H+ | 0 | 11 | 1710 | 1850 | 2090 | 1.41e3, 4.18e-6 |
| | H+ | 15 | 12 | 1200 | 1550 | 1590 | 2.20e3, 5.47e-6 |
| | H+ | 0 | 12 | 1320 | 1920 | 1590 | 1.82e3, 5.61e-6 |
| | H+ | 2 | 12 | 1320 | 1920 | 1570 | 5.28e2, 1.63e-6 |
| | H+ | 15 | 13 | 1090 | 1200 | 1300 | 2.72e3, 5.24e-6 |
| | H+ | 0 | 13 | 1090 | 1200 | 1300 | 1.78e3, 3.43e-6 |
| | H+ | 0 | 13 | 1810 | 2200 | 2300 | 2.45e3, 7.11e-6 |
| | H+ | 0 | 13 | 1090 | 1200 | 1250 | 8.43e2, 1.62e-6 |
| | H+ | 0 | 14 | 1700 | 1880 | 2270 | 1,00e3, 3.01e-6 |

**Table 2** (*continued*)

| Instrument Cycle Number | Species | Azimuth Sector | Elevation Sector | FWHM Low Energy (eV) | Energy at Peak (eV) | FWHM High Energy (eV) | Number Flux at Peak ions/(cm$^2$ s sr eV) |
|---|---|---|---|---|---|---|---|
| 9 | H+ | 0 | 8 | 1100 | 1270 | 1700 | 1.44e3, 2.93e-6 |
| | H+ | 15 | 9 | 750 | 1000 | 1380 | 2.02e3, 3.24e-6 |
| | H+ | 0 | 9 | 750 | 920 | 1000 | 2.97e3. 4.38e-6 |
| | H+ | 0 | 9 | 1380 | 1700 | 1860 | 2.55e3, 6.95e-6 |
| | H+ | 2 | 9 | 890 | 920 | 1380 | 1.02e3, 1.51e-6 |
| | H+ | 0 | 10 | 1600 | 1700 | 1950 | 1.35e3, 3.68e-6 |
| 10 | H+ | 0 | 9 | 870 | 1690 | 2120 | 6.96e2, 1.89e-6 |
| | H+ | 1 | 9 | 1600 | 1830 | 2080 | 2.72e3, 7.98e-6 |
| | H+ | 15 | 10 | 1750 | 1870 | 1930 | 5.87e2, 1.76e-6 |
| | H+ | 15 | 10 | 2250 | 2300 | 2680 | 5.39e2, 1.99e-6 |
| | He++ | 0 | 10 | 1250 | 1420 | 1490 | 9.58e2, 2.18e-6 |
| | H+ | 0 | 10 | 1650 | 2010 | 2330 | 6.81e2, 2.20e-6 |
| | H+ | 0 | 10 | 2550 | 3120 | 3420 | 7.26e2, 3.63e-6 |
| 11 | H+ | 0 | 7 | 2470 | 2880 | 2980 | 6.96e2, 3.22e-6 |
| | H+ | 0 | 8 | 2120 | 3420 | 3880 | 9.18e2, 5.04e-6 |

magnetosheath and solar wind plasma as the coherent plasma structure breaks up into a non-coherent structure. In a sense, this could be an extension of the Brace et al. (1987) description of how the Venus ionosphere breaks up into fragments in its ionotail (see Brace et al., 1987, Figure 4). Since the observation interval started on the nightside where the ionosphere break-up occurs, any wavy motion of the bow shock may also break up the magnetosheath plasma and end up being detected as a separate bow shock crossing as the spacecraft passes through the region. With the limited instrumentation complement on the MEx spacecraft, it is not possible to determine whether the structure is attached to the rest of the bow shock/magnetosheath or detached from the bow shock/magnetosheath. However, in that case of Fig. 2, the ion plasma can no longer be distinguished from the foreshock plasma because the accelerated (reflected) ions are observed throughout the entire region where the break-up occurs.

The plasma measurements indicate the magnetosheath boundary is in transition. In general, the shape of the magnetospheric cavity changes in response to solar wind pressure and the orientation of the IMF. There are three components to this pressure: ion, electron, and magnetic. The electron energy and electron flux values are similar in the solar wind and in the region between measurements of the two magnetosheath locations (e.g. between 2225:30 UT and 2230 UT). This indicates that the change in location of the bow shock is not driven by a change in the electron pressure. Regarding the ions, the ion energy and ion flux values are similar in the solar wind and in the region between 2225:30 UT and 2230 UT as well, indicating that the change in location of the bow shock is not driven by a change in the ion pressure. This suggests that the change in location of the bow shock is due to a change in the magnetic pressure and/or a change in the orientation of the IMF resulting in a reorientation of the magnetospheric cavity. Unfortunately MEx does not contain a magnetic field experiment, so no information about the magnetic field can be determined by MEx. However, since our observations essentially rule out a change in particle pressure, it is most probable that the change in the location of the magnetosheath results from a change in the IMF orientation.

Since it is observed that at this time the magnetic configuration of the magnetospheric boundary is not steady, the boundary could have undergone radical changes in location as long as the locations of the boundary measurements were maintained. This means that when the spacecraft is making measurements in the solar wind, the bow shock location could be at any altitude below the spacecraft as long as it is at the proper location to be detected at 2221 UT. Similarly, when the spacecraft is measuring solar wind plasma between 2225:30 UT and 2230 UT, the location of the bow shock could be at any altitude below the spacecraft as long as it is at the proper location to be detected at 2230 UT.

The ion spectrogram shown in Fig. 4 indicates measurement cycles of IMA as numbered from the appearance of foreshock-like ions in the solar wind to the last location where foreshock-like ions are observed in the magnetosheath. The location of the primary solar wind ion beam is indicated in Table 1. Table 1 is organized to show the location of the solar wind beam in the IMA. For each instrument cycle and ion species, the largest solar wind flux is highlighted in blue. In general it is observed that the primary solar wind beam is located between IMA azimuth sectors 0 and 1, and IMA elevation sectors 7 and 8. After penetrating the magnetosheath, there is a slight shift of the solar wind beam toward IMA azimuth sectors 15 and 0. Table 1 also shows that the peak number flux decreases in general after the first bow shock is encountered except just after the reverse shock at 2226 UT, where the largest value of number flux is observed (cycle 7, 2.78e4 $H^+$ ions/(cm$^2$ s sr eV)). The ion number flux measurement just before the final bow shock is encountered (cycle 8) is about 3 times less (8.80e3 $H^+$ ions/(cm$^2$ s sr eV)) than the previous cycle and almost half the hydrogen number flux early in the solar wind.

There should be an obvious change in direction between the flow in the solar wind and that in the magnetosheath. The average location and shape of the bow shock suggest that the solar wind inside the magnetosheath is flowing with an angle of about 30°

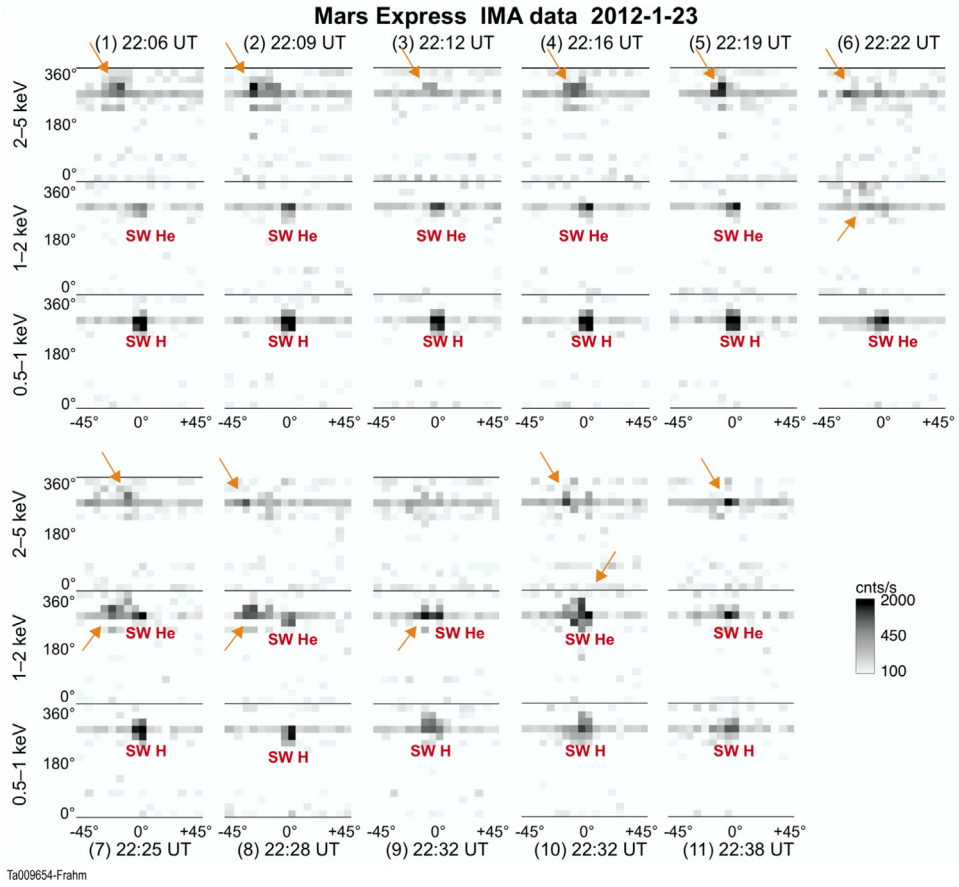


**Fig. 5.** Instrument angular view. Shown are 11 angular view spectrograms corresponding to the cycles marked in Fig. 4. Each are marked with the approximate center time of the measurement cycle and the cycle number. Along each vertical axis is the instrument azimuth rotated by 180° to display the solar wind in the center (0°–360°) and each horizontal axis is the instrument elevation (−45° to +45°). Angular spectrograms for three integral energy bands (0.5–1 keV, 1–2 keV, and 2–5 keV) are shown in a stacked configuration. Locations of the solar wind (SW) hydrogen (H) and helium (He) are indicated. Arrows point to foreshock/foreshock-like ions.

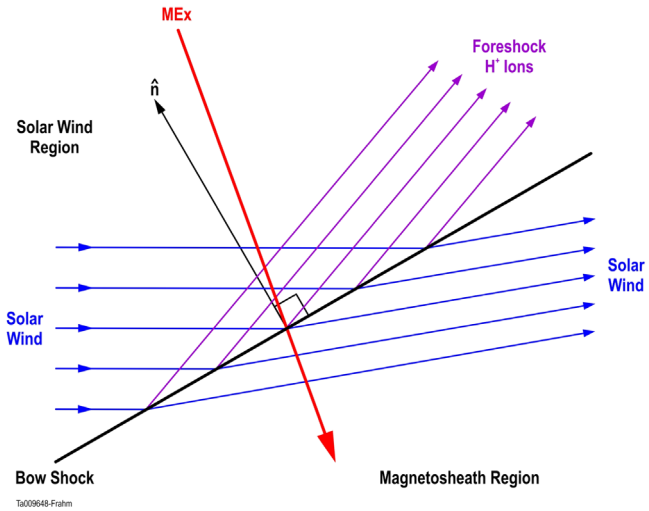


**Fig. 6.** Creation of foreshock ions at the bow shock. The solar wind (blue) intersects the bow shock (black) creating a transmitted component (blue) of solar wind ions and a reflected component (purple) of foreshock ions (after Yamauchi et al., 2015). Reflected ions are accelerated by an electric field in the bow shock due to the magnetic field and solar wind velocity causing the foreshock ions to have energies that are multiples of the solar wind energy.

with respect to the Mars–Sun line. From the discussion in the previous paragraph, the rotation in azimuth represents a 22.5° change. Observations shown in Table 1 indicate that the solar wind changes elevation from sector 7 to sector 8 when the spacecraft transitions, so that is at most a change of about 5.6°. Thus, it is plausible that the shift in flow directions from the solar wind to the magnetosheath was observed in the ion data. An obvious transition is probably observed but not as distinct due to the orientation of the ion instrument at the time the bow shock was encountered.

Since the measurements of the solar wind ion flux within the region between the two magnetosheath crossings (2225:30 UT to 2230 UT of Fig. 4) show such different values of the solar wind ion flux than the first cycle in the magnetosheath (cycle 6), it is worth examining them to determine if changes in the $H^+$ peak number flux could drive a fluctuation of the location of the bow shock. If the solar wind is steady, then the first bow shock encounter (2221 UT) is taken as the normal location of the bow shock. If the solar wind number flux increased as in cycle 7, more pressure would be exerted on the magnetosheath and a compressed magnetosphere would be expected as the initial reaction. This could cause the bow shock to overtake the spacecraft and appear at a lower altitude. However, the $H^+$ flux recorded in cycle 8 is less than the average solar wind value, so with this same logic, one would expect the bow shock to move to higher altitude and have overtaken MEx by the time IMA had made its measurement. Thus, this solution presents inconsistent arguments. The number flux increase observed in cycle 7 did not lead to a pressure increase.

The foreshock-like ions circled in the ion spectrogram of Fig. 4 are listed in Table 2. These foreshock ions are observed both in the solar wind and in the region signified by the shocked solar wind electron plasma. In the solar wind, the foreshock-like ions form a well defined, narrow feature about 20° from the solar wind direction and coming from the direction of the planet. These ions

are tracked from the solar wind through the bow shock and into the magnetosheath, indicating penetration of the solar wind. During the encounter with the planet, foreshock-like ions are observed at energies greater than the solar wind proton energy. The foreshock-like ions are identified in the mass spectra as continuous peaks in the differential number flux spectra which were above the level of scattered ion flux. Scattered ions are identified near the instrument count and number flux thresholds with a large energy range and are observed to increase inside the magnetosheath, indicating ion scattering by the bow shock. Foreshock-like ions were identified as features in the spectrum which had a full-width-at-half-maximum above the scattered ion level. The differential energy flux is estimated based on the center energy and differential number flux at the peak. The differential energy flux values are examined within an instrument cycle, and the largest value is highlighted in blue.

The foreshock-like ions are also observed in Fig. 7. Shown in Fig. 7 are energy-time spectrograms from the five IMA azimuth sectors which point toward the Sun. The electron energy-time spectrogram is shown at the top for reference. Spectrograms are presented in differential energy flux with color bars for ions and electrons at the right where ion fluxes less than 5.0e−7 ergs/(cm$^2$ s sr eV) have been removed. Fig. 7 shows that the ions are clustered near the solar pointing sectors. After 2240 UT, Fig. 7 also shows that the solar wind that has penetrated the magnetosheath has been heated (because of the increased spread in energy), dispersing in angle from its cold beam structure. The loss of azimuthal angular extent toward the IMB and the restriction of the ions to nearly the same elevations indicates that the magnetosheath ions are flowing away from the planet. As indicated by Fig. 2, the thickness of the magnetosheath is about 4000 km, or about 4 times the proton gyroradius in the solar wind. Thus, there are two distinct regions in the magnetosheath which are an outer layer, within a proton gyroradius from the bow shock in which the solar wind ions remain cold, and the inner region of the magnetosheath where the ions are heated.

Examining Table 2, one sees that the locations of the foreshock-like ions are found consistently in elevation sectors greater than the sector containing the proton beam, and azimuth sectors are approximately the same as those of the solar wind $H^+$ beam, except for instrument cycles 4 and 11. Instrument cycle 4 occurs in the solar wind before the first encounter with a bow shock, and cycle 11 is the last instrument cycle which shows foreshock-like ions. For cycle 11, no elevation sectors other than that which shows the solar wind beam are observed. Foreshock ions are observed in larger sectors in cycle 4. The second largest value of energy flux within cycle 4 is highlighted in yellow. The amount of energy flux is about half that of the largest value and occurs during the largest elevation sector that shows foreshock-like ions. Also highlighted in yellow, the second largest energy flux of cycles 5 and 10 also occur during the largest elevation sector for each cycle that shows foreshock-like ions. Thus, these foreshock-like ions flow from the direction of the solar wind in azimuth and have a component that flows from the planet away from the Mars ecliptic. In other words, these foreshock-like ions most likely are reflected off the bow shock at a location toward the front of the magnetosphere and are deflected into the instrument. Foreshock-like ions in elevation sector 11 are most likely generated at a location closer to the spacecraft and come from the direction of the solar wind. Ions that appear behind the bow shock may be due to the chaotic nature of the magnetic cavity in the encountered region.

Although foreshock-like ions are mostly observed to be protons, foreshock-like ions in the solar wind and in the magnetosheath do not appear as ring distributions as shown in Yamauchi et al. (2006, 2008, 2011, 2012) despite being detected by the same instrumentation. The IMA location of the largest observed flux indicates that the instrument would have the capability to detect a ring if one were present. The distributions are not diffuse outside the foreshock but remain beam-like when detected. There is some blockage by the spacecraft and at this time, that blockage occurs in elevations which are detecting ions flowing toward the planet (elevations less than 6) from the Mars ecliptic plane (azimuths greater than 8), which is about a fourth of the measured volume. Thus in the solar wind, IMA would be unable to determine if there were ions flowing around the planet from the equator of Mars toward its southern pole, but could measure ions if they were flowing in the opposite direction.

An additional explanation for the penetration depth may be due to the ion gyroradius. Assuming a 10 nT IMF and a 750 eV $H^+$ ion, the gyroradius is about 800 km. This is about the altitude difference between the electron bow shock and the point at which the last foreshock-like ions are observed (cycle 11). If ions are generated at the bow shock within a gyroradius depth, they could be following the magnetic field, and the elevation at which the foreshock-like ions are observed could be reflecting the pitch angle of the foreshock-like ions. In this case, foreshock-like ions are expected to be gyrotropic and to exist in additional elevation-azimuth combinations if frozen-in flux is assumed. However, the frozen-in condition is violated on small distance scales within plasma boundaries like the bow shock. Different populations of ions have been observed in the Earth's magnetosheath at the same time flowing in different directions in the presence of a magnetic field (Lundin et al., 1987; Lundin 1997). The electron spectrogram indicates the presence of waves in the magnetosheath, so it is possible that a portion of the solar wind proton beam could be reflected by wave–particle reactions inside the magnetosheath.

An additional issue is that foreshock-like ions may be gyrophase bunched. If this were the case, one would expect that the location of the detected gyro bunch to drift in azimuth-elevation location as MEx penetrates into the magnetosphere because of the difference in location at which the foreshock-like ions would be reflected. This is not observed.

## 6. Future studies

Although this paper presented foreshock-like ions which were observed in both the foreshock region and in the magnetosheath, there have been some observations of ions in the foreshock region which are not observed in the magnetosheath (the traditional foreshock ions). An example of this is shown in Figs. 8 and 9 on April 2, 2012, from 2210 UT until 2140 UT. Here, the spacecraft orbit shown in Fig. 8 was similar to that shown in Fig. 1, but the spacecraft had precessed further into the night side. The average locations of the bow shock (about 2020 UT) and MPB (about 2134 UT) are further from the planet than the electron data indicate. The actual features were crossed by the spacecraft as shown in Fig. 8d and indicated on the top of the spectrogram shown in Fig. 9 (note that the electron data does not unambigously indicate when the IMB is crossed during this spacecraft pass). The attitude was a bit different as well, resulting in the ion detection at different azimuth sectors as well as ions in the foreshock region as shown in Fig. 9, observed in different elevation sectors than those shown in Fig. 2. On April 2, the solar wind $H^+$ appears mostly in azimuth sectors 0 and 1 where the proton beam is intense enough to extend above the threshold in sector 2, but the $He^{++}$ distribution does not have enough intensity to exceed the count threshold. The solar wind $H^+$ and $He^{++}$ ions are again indicated in the first three instrument cycles in sector 1 of Fig. 9. The energy spread in the solar wind ions begins at about 2039 UT indicated shocked ion plasma. This occurs closer to the planet than the average bow shock location, which

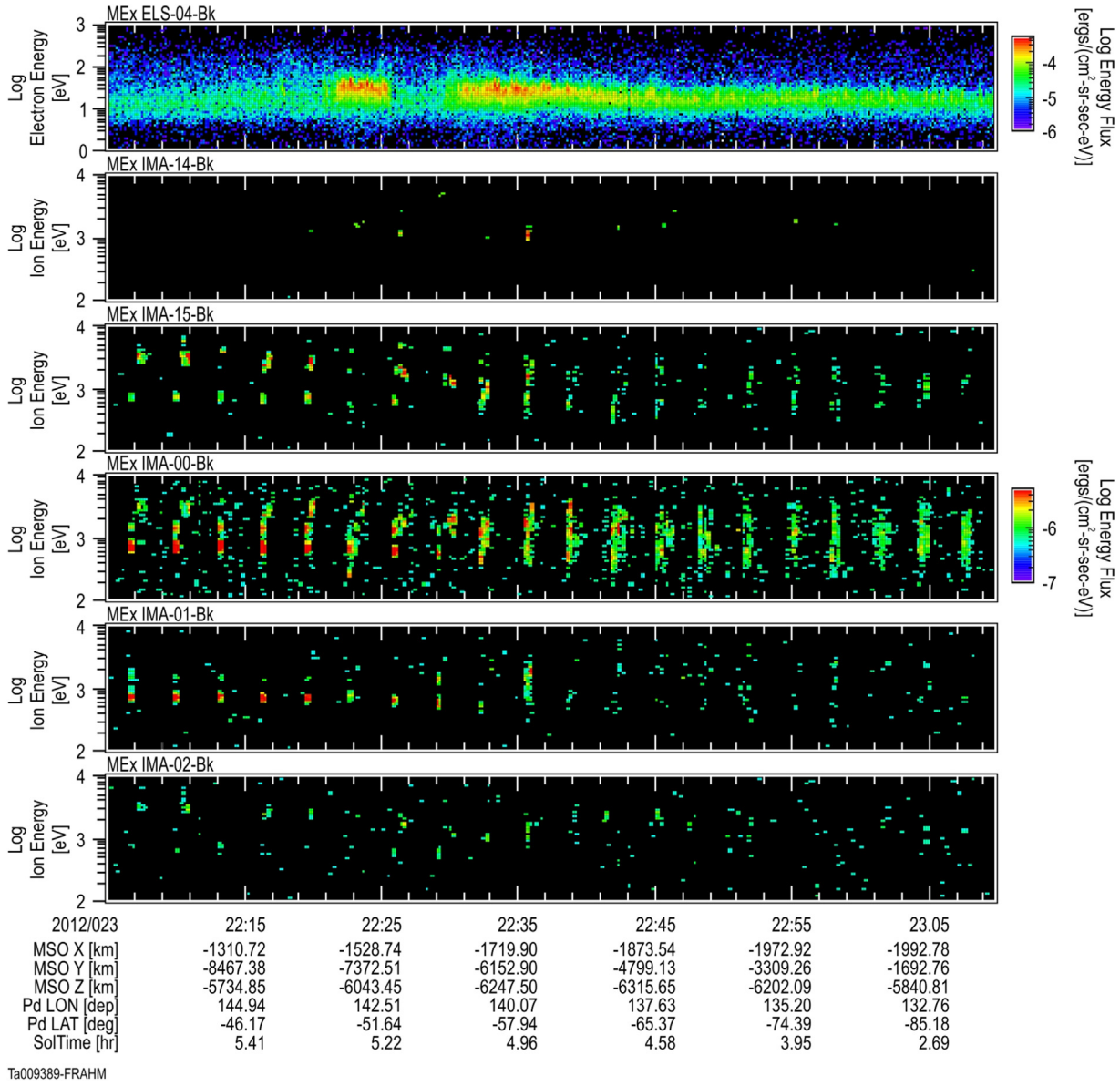


**Fig. 7.** Ions in the magnetosheath. The bottom five panels contain ion energy-time spectrograms of the differential energy flux from IMA azimuth sectors 14, 15, 0, 1, and 2 which have background removed, all with the same color scale at the right. Ion energy flux values below 5.0e−7 ergs/(cm$^2$ s sr eV) are excluded. An electron energy-time sperctrogram of the electrons from ELS sector 4 also in differential energy flux with background removed, is shown for reference in the top panel.

should have been crossed about 2020 UT. Heated ion plasma is observed in the magnetosheath compared to the cold solar wind. There was almost no significant number of ions flowing at elevations different from the solar wind. Ions of energy greater than 3 keV were also observed in the foreshock region from 2013 UT until 2032 UT above 3 keV at elevations less than the solar wind beam as seen in sector 2 of Fig. 9. Instead of being fairly constant in energy as in the previous example, in this case the ion energy increased with distance away from the bow shock.

The electrons showed multiple crossings of the bow shock like Fig. 2 and the presence of wave activity. Solar wind electrons are observed until 2030 UT at which time there is a slight increase in electron energy, indicating the appearance of the electron foreshock region. From 2034 UT until 2054 UT, there are at least 7 crossings of the bow shock indicated by a difference between shocked solar wind core electrons on one side of a bow shock and foreshock electrons on the opposite side of a bow shock. After 2054 UT, the shocked solar wind core electron population is observed, indicating the spacecraft is inside of the magnetosheath. Whenever magnetosheath electron plasma is observed, variations in the energy range and intensity of the electron population indicate the presence of wave activity. Most of the 7 electron bow shock crossings are shorter than an ion instrument cycle and the solar wind ions show heating; however, there exists one ion instrument cycle between 2044 UT and 2048 UT which suggests that the ions observed in sectors 0 and 1 are similar to cold ions in the solar wind. The previous pass the electrons show no multiple bow shock crossing in the electrons and the next pass shows two. The electrons show no multiple bow shock crossings on the following pass. Fig. 9 indicates that the bow shock can at times be a complicated structure. Multiple bow shock crossings could provide more opportunities to generate foreshock ions as they scatter from boundary regions; however, in this case foreshock-like ions were not observed in the magnetosheath as was the situation on January 23 (Fig. 2).

Future studies should look at the conditions which lead to observations of both multiple bow shock crossings and the locations of foreshock-like ions. Foreshock-like ions inside the

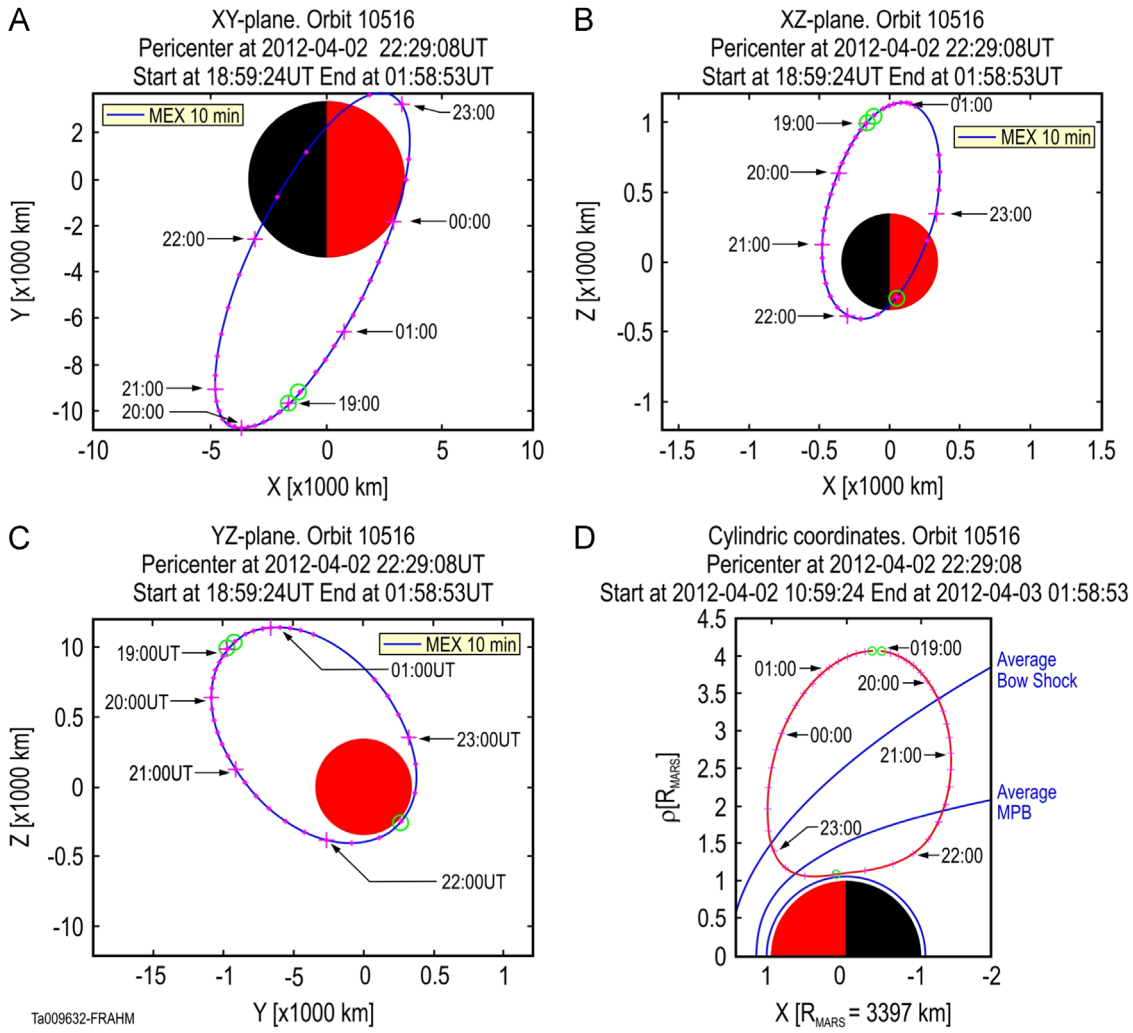


**Fig. 8.** Mars Express Trajectory on 2 April 2012 in the same format as Fig. 1. The orbit of the spacecraft has precessed to sample plasma from deeper on the night side of the planet.

magnetosheath appear not to be caused by multiple crossings of the bow shock. This study should also include where and when both are observed, with the objective of explaining why some ions are observed at constant energy while others are not. For example, no cases of multiple bow shock crossings or foreshock-like ions were observed by IMA in 2004 and 2005 when the solar cycle was approaching solar minimum; however, IMA observed both foreshock-like ions inside and outside the magnetosheath in 2012 as solar maximum was approaching, despite coverage of the same spatial region in both time intervals.

Since the region inside the bow shock where foreshock-like ions are observed is about a proton gyroradius, studies of wave–particle interactions also need to determine the effect of wave activity on the presence or absence of foreshock-like ions in the magnetosheath. Such studies should discuss the differences in wave activity and ion flow between the outer magnetosheath where foreshock-like ions are observed and the inner magnetosheath where they are not observed. Wave activity could be extended to look at the role of the magnetic field. Wave activity generated in quasi-perpendicular shocks could be contrasted with quasi-parallel shocks to determine how the extraction of foreshock-like ions occurs. It is possible that ions in the foreshock region are liberated from the bow shock based on only gyromotion. Again, these effects should be investigated.

Lastly, this paper discusses foreshock-like ions that are very finite in angle. It is not clear if or how these ions are related to those exhibiting cycloidal motion. It is possible that ions exhibit a cycloidal motion near the front of the Martian bow shock and morph into a beam-like structure as they progress down the tail.

## 7. Conclusion

Ions in the foreshock region of Mars were observed by the particle detectors on MEx on 23 January 2012 between 2205 UT and 2221 UT. On this pass, the MEx spacecraft was moving inbound from the solar wind in the southern hemisphere from dawn, reaching periapsis on the dusk side of Mars near the equator at about 350 km altitude. The foreshock-like ions were observed to penetrate through multiple bow shock crossings and into the magnetosheath of Mars (to 2240 UT). Plasma measurements indicated that MEx crossed the bow shock three times while inbound from the solar wind (between 2221 UT and 2230 UT) with the solar wind reappearing just before the last bow shock crossing. The multiple bow shock crossing was determined to be a transient feature based on additional passes through the same spatial region near the time of the measurements and multiple crossings over many years. Changes in the ion and electron pressure was not the cause of the bow shock location change, but

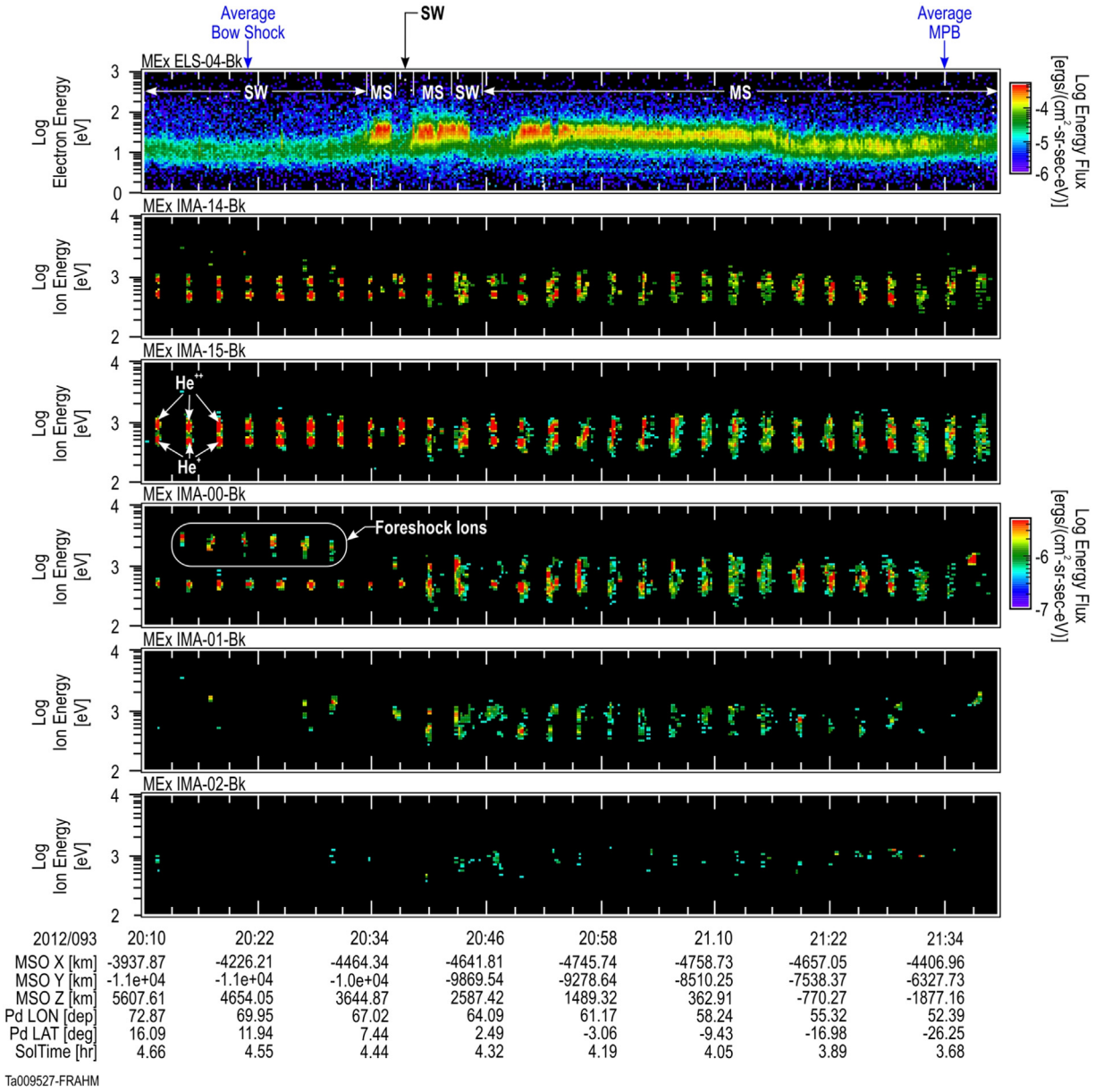


**Fig. 9.** Ions in the Foreshock. The format is the same as Fig. 7; however, the IMA sectors 0, 1, 2, 3, and 4 (which show significant fluxes) are different from Fig. 7.

magnetic pressure and IMF orientation cannot be ruled out as a possible cause.

Ions in the foreshock of the solar wind were observed to be beam-like around 20° from the solar wind direction. The ions had energies several times that of the solar wind protons. Foreshock-like ions were observed to penetrate into the magnetosheath and were observed until MEx was about a proton gyroradius from the bow shock. Shocked electron plasma indicated the presence of waves in the magnetosheath which could be reflecting a portion of the solar wind protons. It is expected that the frozen-in-flux assumption is violated within the bow shock region which would allow plasma to be generated at different angles to the magnetic field, allowing wave–particle interactions to generate the foreshock-like ion beams which are then transported into the foreshock region. The foreshock ions reflected from the bow shock are produced at a location upstream of the spacecraft while the spacecraft is in the solar wind. Foreshock-like ions could be locally produced deep inside the magnetosheath or at a location which is temporarily closer to the planet than the detected bow shock location.

It was observed that on this pass, ions in the magnetosheath could be separated into those within a proton gyroradius from the bow shock and those nearer the IMB. Those near the bow shock still retained their cold beam-like structure while those toward the IMB were heated and flowed along the magnetosheath, in the direction of the tail of the magnetosphere.

## Acknowledgments

The ASPERA-3 experiment on the European Space Agency (ESA) Mars Express mission is a joint effort between 15 laboratories in 10 countries, all sponsored by their national agencies. We thank all of these agencies as well as the various departments/institutions hosting these efforts. We wish to acknowledge support through the National Aeronautics and Space Administration (NASA) Contract NASW-00003 in the United States, Science and Technology

Facilities Council (STFC) in the United Kingdom, and the Swedish National Space Board for their support of the PI-Institute.

## References


Bale, S.D., Balikhin, M.A., Horbury, T.S., Krasnoselskikh, V.V., Kucharek, H., Mobius, E., Walker, S.N., Balogh, A., Burgess, D., Lembege, B., Lucek, E.A., Scholer, M., Schwartz, S.J., Thomsen, M.F., 2005. Quasi-perpendicular shock structure and processes. Space Sci. Rev. 118, 161–203. http://dx.doi.org/10.1007/s11214-005-3827-0.

Barabash, S.R., Lundin, H., Andersson, J., Gimholt, M., Holmström, O., Norberg, M., Yamauchi, K., Asamura, A.J., Coates, D.R., Linder, D.O., Kataria, C.C., Curtis, K.C., Hsieh, B.R., Sandel, A., Fedorov, A., Grigoriev, E., Budnik, M., Grande, M., Carter, D.H., Reading, H., Koskinen, E., Kallio, P., Riihelä, T., Säles, J., Kozyra, N., Krupp, S., Livi, J., Woch, J., Luhmann, S., McKenna-Lawlor, S., Orsini, R., Cerulli-Lrelli, M., Maggi, A., Morbidini, A., Mura, A., Milillo, E., Roelof, D., Williams, J.-A., Sauvaud, J.-J., Thocaven, T., Moreau, D., Winningham, R., Frahm, J., Scherrer, J., Sharber, P., Wurz, Bochsler, P., 2004. ASPERA-3: Analyser of Space Plasmas and Energetic Ions for Mars Express, MARS EXPRESS: The Scientific Payload SP-1240. Wilson, A. (Ed.), 2004. European Space Agency Publications Division, European Space Research & Technology Centre, Noordwijk, The Netherlands, pp. 121–139.

Barabash, S., Lundin, R., Andersson, H., Brinkfeldt, K., Grigoriev, A., Gunell, H., Holmström, M., Yamauchi, M., Asamura, K., Bochsler, P., Wurz, P., Cerulli-Irelli, R., Mura, A., Milillo, A., Maggi, M., Orsini, S., Coates, A.J., Linder, D.R., Kataria, D. O., Curtis, C.C., Hsieh, K.C., Sandel, B.R., Frahm, R.A., Sharber, J.R., Winningham, J. D., Grande, M., Kallio, E., Koskinen, H., Riihelä, P., Schmidt, W., Säles, T., Kozyra, J. U., Krupp, N., Woch, J., Livi, S., Luhmann, J.G., McKenna-Lawlor, S., Roelof, E.C., Williams, D.J., Sauvaud, J.-A., Fedorov, A., Thocaven, J.-J., 2006. The Analyzer of Space Plasmas and Energetic Atoms (ASPERA-3) for the Mars Express mission. Space Sci. Rev. 26, 113–164.

Brace, L.H., Kasprzak, W.T, Taylor, H.A., Theis, R.F., Russell, C.T., Barnes, A., Mihalov, J.D., Hunten, D.M., 1987. The ionotail of Venus: Its configuration and evidence for ion escape. J. Geophys. Res. 92, 15–26. http://dx.doi.org/10.1029/JA092iA01p00015.

Brain, D.A., Bagenal, F., Acuña, M.H., Connerney, J.E.P., 2003. Martian magnetic morphology: contributions from the solar wind and crust. J. Geophys. Res. 108, 1424. http://dx.doi.org/10.1029/2002JA009482.

Burgess, D., Schwartz, S.J., 1984. The dynamics and upstream distributions of ions reflected at the Earth's bow shock. J. Geophys. Res. 89, 7407–7422.

Burgess, D., Lucek, E.A., Scholer, M., Bale, S.D., Balikhin, M.A., Balogh, A., Horbury, T.S., Krasnoselskikh, V.V., Kucharek, H., Lembège, B., Möbius, E., Schwartz, S.J., Thomsen, M.F., Walker, S.N., 2005. Quasi-parallel shock structure and processes. Space Sci. Rev. 118, 205–222. http://dx.doi.org/10.1007/s11214-005-3832-3.

Burgess, D., 1995. Collisonless shocks. In: Kivelson, M.G., Russell, C.T. (Eds.), Introduction to Space Physics. Cambridge University Press, Cambridge, UK, pp. 129–163.

Chicarro, A., Martin, P., Trautner, R., 2004. The Mars Express mission: An overview, MARS EXPRESS: The Scientific Payload SP-1240. Wilson, A. (Ed.), 2004. European Space Agency Publications Division, European Space Research & Technology Centre, Noordwijk, The Netherlands, pp. 3–13.

Coates, A.J., 2012. Ion pickup and acceleration: measurements from planetary missions, Physics of the Heliosphere: A 10-year Retrospective 978-0-7354-1026-8. Heerikhuisen, J., Li, G., Pogorelov, N., Zank, G. (Eds.), AIP 10th Annual Astrophysics Conference Proceedings, 1436; 2012, pp. 89–102.

Connerney, J.E.P., Acuña, M.H., Wasilewski, P.J., Kletetschka, G., Ness, N.F., Rème, H., Lin, R.P., Mitchell, D.L., 2001. The global magnetic field of Mars and implications for crustal evolution. Geophys. Res. Lett. 28, 4015–4018. http://dx.doi.org/10.1029/2001GL013619.

Crider, D.H., Vignes, D., Krymskii, A.M., Breus, T.K., Ness, N.F., Mitchell, D.L., Slavin, J. A., Acuña, M.H., 2003. A proxy for determining solar wind dynamic pressure at Mars using Mars Global Surveyor data. J. Geophys. Res. 108, 1461. http://dx.doi.org/10.1029/2003JA009875.

Eastwood, J.P., Lucek, E.A., Mazelle, C., Meziane, K., Narita, Y., Pickett, J., Treumann, R.A., 2005. The foreshock. Space Sci. Rev. 118, 41–94. http://dx.doi.org/10.1007/s11214-005-3824-3.

Espley, J.R., Cloutier, P.A., Brain, D.A., Crider, D.H., Acuña, M.H., 2004. Observations of low-frequency magnetic oscillations in the martian magnetosheath, magnetic pileup region, and tail. J. Geophys. Res. 109, A07213. http://dx.doi.org/10.1029/2003JA010193.

Espley, J.R., Cloutier, P.A., Crider, D.H., Brain, D.A., Acuña, M.H., 2005. The October 2003 solar storm A09S33. J. Geophys. Res. 110. http://dx.doi.org/10.1029/2004JA010935.

Feynman, J., 1985. ADA 167000. Jursa, A.S. (Ed.), Solar Wind, Handbook of Geophysics and the Space Environment. Air force Geophysics Laboratory.

Frahm, R.A., Winningham, J.D., Sharber, J.R., Scherrer, J.R., Jeffers, S.J., Coates, A.J., Linder, D.R., Kataria, D.O., Lundin, R., Barabash, S., Holmström, M., Andersson, H., Yamauchi, M., Grigoriev, A., Kallio, E., Säles, T., Riihelä, P., Schmidt, W., Koskinen, H., Kozyra, J.U., Luhmann, J.G., Roelof, E.C., Williams, D.J., Livi, S., Curtis, C.C., Hsieh, K.C., Sandel, B.R., Grande, M., Carter, M., Sauvaud, J.-A., Fedorov, A., Thocaven, J.-J., McKenna-Lawler, S., Orsini, S., Cerulli-Irelli, R., Maggi, M., Wurz, P., Bochsler, P., Krupp, N., Woch, J., Fränz, M., Asamura, K., Dierker, C., 2006a. Carbon dioxide photoelectron energy peaks at Mars. Icarus 182, 371–382.

Frahm, R.A., Sharber, J.R., Winningham, J.D., Wurz, P., Liemohn, M.W., Kallio, E., Yamauchi, M., Lundin, R., Barabash, S., Coates, A.J., Linder, D.R., Kozyra, J.U., Holmström, S., Jeffers, S.J., Andersson, H., McKenna-Lawler, S., 2006b. Locations of atmospheric photoelectron energy peaks within the Mars environment. Space Sci. Rev. 126, 389–402.

Frahm, R.A., Kallio, E., Futaana, Y., Fedorov, A., Janhunen, P., 2008. Variations of the magnetic field near Mars caused by magnetic crustal anomalies. Planet. Space Sci. 56, 856–860. http://dx.doi.org/10.1016/j.pss.2007.12.018.

Frahm, R.A., Sharber, J.R., Winningham, J.D., Link, R., Liemohn, M.W., Kozyra, J.U., Coates, A.J., Linder, D.R., Barabash, S., Lundin, R., Fedorov, A., 2010. Estimation of the escape of photoelectrons from Mars in 2004 liberated by the ionization of carbon dioxide and atomic oxygen. Icarus 206, 50–63. http://dx.doi.org/10.1016/j.icarus.2009.03.024.

Gunell, H.H., Nilsson, G., Stenberg, M., Hamrin, T., Karlsson, R., Maggiolo, M., Andre, R., Lundin, Dandouras, I., 2012. Plasma penetration of the dayside magnetopause. Phys. Plasmas 19 (072906), 1–11. http://dx.doi.org/10.1063/1.4739446.

Hietala, H., Partamies, N., Laitinen, T.V., Clausen, L.B.N., Facskó, G., Vaivads, A., Koskinen, H.E.J., Dandouras, I., Rème, H., Lucek, E.A., 2012. Supermagnetosonic subsolar magnetosheath jets and their effects: from the solar wind to the ionospheric convection. Ann. Geophys. 30, 33–48. http://dx.doi.org/10.5194/angeo-30-33-2012.

Kallio, E., Fedorov, A., Budnik, E., Barabash, S., Jarvinen, R., Janhunen, P., 2008. On the properties of $O^+$ and $O_2^+$ ions in a hybrid model and in Mars Express IMA/ASPERA-3 data: a case study. Planet. Space Sci. 56, 1204–1213.

Luhmann, J.G., 1995. Plasma interactions with unmagnetized bodies. In: Physics (Ed.), Introduction to Space. Cambridge University Press, Cambridge, UK, pp. 203–225.

Lundin, R., Stasiewicz, K., Hultqvist, B., 1987. On the interpretation of different flow vectors of different ion species in the magnetospheric boundary layer. J. Geophys. Res. 92, 3214–3222. http://dx.doi.org/10.1029/JA092iA04p03214.

Lundin, R., Barabash, S., Andersson, H., Holmström, M., Grigoriev, A., Yamauchi, M., Sauvaud, J.-A., Fedorov, A., Budnik, E., Thocaven, J.-J., Winningham, D., Frahm, R., Scherrer, J., Sharber, J., Asamura, K., Hayakawa, H., Coates, A., Linder, D.R., Curtis, C., Hsieh, K.C., Sandel, B.R., Grande, M., Carter, M., Reading, D.H., Koskinen, H., Kallio, E., Riihela, P., Schmidt, W., Säles, T., Kozyra, J., Krupp, N., Woch, J., Luhmann, J., McKenna-Lawler, S., Cerulli-Irelli, R., Orsini, S., Maggi, M., Mura, A., Milillo, A., Roelof, E., Williams, D., Livi, S., Brandt, P., Wurz, P., Bochsler, P., 2004. Solar wind-induced atmospheric erosion at Mars: first results from ASPERA-3 on Mars Express. Science 305, 1933–1936. http://dx.doi.org/10.1126/science.1101860.

Lundin, R., Winningham, D., Barabash, S., Frahm, R., Andersson, H., Holmström, M., Grigoriev, A., Yamauchi, M., Borg, H., Sharber, J.R., Sauvaud, J.-A., Fedorov, A., Budnik, E., Thocaven, J.-J., Asamura, K., Hayakawa, H., Coates, A.J., Linder, D.R., Kataria, D.O., Curtis, C., Hsieh, K.C., Sandel, B.R., Grande, M., Carter, M., Reading, D.H., Koskinen, H., Kallio, E., Riihelä, P., Schmidt, W., Säles, T., Kozyra, J., Krupp, N., Woch, J., Fränz, M., Luhmann, J., McKenna-Lawler, S., Cerulli-Irelli, R., Orsini, S., Maggi, M., Roelof, E., Williams, D., Livi, S., Brandt, P.C.:son, Wurz, P., Bochsler, P., 2006. Ionospheric plasma acceleration at Mars: ASPERA-3 results. Icarus 182, 308–319.

Lundin, R., 1997. Observational and theoretical aspects of processes (other than merging and diffusion) governing plasma transport across the magnetopause. Space Sci. Rev. 80, 269–304.

Mazelle, C., Meziane, K., LeQueau, D., Wilber, M., Eastwood, J.P., Reme, H., Sauvaud, J.A., Bosqued, J.M., Dandouras, I., McCarthy, M., Kistler, L.M., Klecker, B., Korth, A., Bavassano-Cattaneo, M.B., Pallocchia, G., Lundin, R., Balogh, A., 2003. Production of gyrating ions from nonlinear wave–particle interaction upstream from the Earth's bow shock: a case study from Cluster-CIS. Planet. Space Sci. 51, 785–795. http://dx.doi.org/10.1016/j.pss.2003.05.002.

Meziane, K., Mazelle, C., Lin, R.P., LeQuéau, D., Larson, D.E., Parks, G.K., Lepping, R.P., 2001. Three-dimensional observations of gyrating ion distributions far upstream from the Earth's bow shock and their association with low-frequency waves. J. Geophys. Res. 106, 5731–5742. http://dx.doi.org/10.1029/2000JA900079.

Oka, M., Terasawa, T., Saito, Y., Mukai, T., 2005. Field-aligned beam observations at the quasi-perpendicular bow shock: generation and shock angle dependence. J. Geophys. Res. 110, A05101. http://dx.doi.org/10.1029/2004JA010688.

Otto, A., 2006. Magnetospheric Physics. Geophysical Institute, University of Alaska ⟨http://how.gi.alaska.edu/ao/msp⟩.

Pachmann, G., Sckopke, N., Papamastorakis, I., Asbridge, J.R., Bame, S.J., Gosling, J.T., 1981. Characteristics of reflected and diffuse ions upstream from the Earth's bow shock. J. Geophys. Res. 86, 4355–4364.

Parks, G.K., 2004. Physics of Space Plasmas. Westview Press, Boulder, Colorado.

Vignes, D., Mazelle, C., Reme, H., Acuña, M.H., Connerney, J.E.P., Lin, r P., Mitchell, D. L., Cloutier, P., Crider, D.H., Ness, N.F., 2000. The solar wind interaction with Mars: Locations and shapes of the bow shock and the magnetic pile-up boundary from the observations of the MAG/ER Experiment onboard Mars Global Surveyor. Geophys. Res. Lett. 27, 49–52. http://dx.doi.org/10.1029/1999GL010703.

Winningham, J.D., Frahm, R.A., Sharber, J.R., Coates, A.J., Linder, D.R., Soobiah, Y., Kallio, E., Espley, J.R., Lundin, R., Barabash, S., Holmström, M., Andersson, H., Yamauchi, M., Grigoriev, A., Scherrer, J.R., Jeffers, S.J., Kataria, D.O., Kozyra, J.U., Luhmann, J.G., Roelof, E.C., Williams, D.J., Livi, S., Curtis, C.C., Hsieh, K.C., Sandel, B.R., Koskinen, H., Säles, T., Riihelä, P., Schmidt, W., Grande, M., Carter, M., Sauvaud, J.-A., Fedorov, A., Thocaven, J.-J., McKenna-Lawler, S., Orsini, S., Cerulli-Irelli, R., Maggi, M., Wurz, P., Bochsler, P., Krupp, N., Woch, J., Fränz, M., Asamura, K., Dierker, C., 2006. Electron oscillations in the induced martian magnetosphere. Icarus 182, 360–370.

Yamauchi, M., Futaana, Y., Fedorov, A., Dubinin, E., Lundin, R., Sauvaud, J.-A., Winningham, J.D., Frahm, R.A., Barabash, S., Holmström, M., Woch, J., Fränz, M.,

Budnik, S., Borg, H., Sharber, J.R., Coates, A.J., Soobiah, Y., Koskinen, H., Kallio, E., Asamura, K., Hayakawa, H., Curtis, C., Hsieh, K.C., Sandel, B.R., Grande, M., Grigoriev, A., Wurz, P., Orsini, S., Brandt, P., Mckenna-Lawler, S., Kozyra, J., Luhmann, J., 2006. IMF, 2006. direction derived from cycloid-like ion distributions observed by Mars Express. Space Sci. Rev. 126, 239–266.

Yamauchi, M., Futaana, Y., Fedorov, A., Kallio, E., Frahm, R.A., Lundin, R., Sauvaud, J.-A., Winningham, J.D., Barabash, S., Holmström, M., 2008. Advanced method to derive the IMF direction near Mars from cycloidal proton distributions. Planet. Space Sci. 56, 1145–1154. http://dx.doi.org/10.1016/j.pss.2008.02.012.

Yamauchi, M., Futaana, Y., Fedorov, A., Frahm, R.A., Winningham, J.D., Dubinin, E., Lundin, R., Barabash, S., Holmström, M., Mazelle, C., Sauvaud, J.-A., Zhang, T.L., Baumjohann, M., Coates, A.J., Fränz, M., 2011. Comparison of accelerated ion populations observed upstream of the bow shocks at Venus and Mars. Ann. Geophys. 29, 511–528. http://dx.doi.org/10.5194/angeo-29–511-2011.

Yamauchi, M., Futaana, Y., Fedorov, A., Frahm, R.A., Dubinin, E., Lundin, R., Sauvaud, J.-A., Winningham, J.D., Barabash, S., Holmström, M., 2012. Ion acceleration by multiple reflections at Martian bow shock. Earth Planets Space 64, 61–71.

Yamauchi, M., Lundin, R., Frahm, R.A., Sauvaud, J.-A., Holmström, M., Barabash, S., 2015. Oxygen foreshock of Mars. Planet. Space Sci. 119, 48–53. http://dx.doi.org/10.1016/j.pss.2015.08.003.